

Scaling Laws of Fracture Network Properties in Crystalline Rock: a Powerful Approach to the Characterization of Unconventional Geofluids Reservoirs

Alberto Ceccato¹, GIULIA Tartaglia¹, Marco Antonellini¹, and Giulio Viola²

¹University of Bologna

²Dipartimento di Scienze Biologiche, Geologiche ed Ambientali, Università degli Studi di Bologna

November 21, 2022

Abstract

The multiscale analysis of fracture patterns helps to define the geometric scaling laws and the genetic relationships correlating outcrop- and regional-scale structures in a fracture network. Here we present the results of the multiscale analysis of the geometrical and spatial organization properties of the fracture network affecting the Rolvsnes granodiorite of the crystalline basement of southwestern Norway (Bømlo island). The fracture network shows a spatial distribution described by a fractal dimension D [?] 1.51, with fracture lengths distributed following a power-law scaling law (exponent $\alpha = -1.95$). However, orientation-dependent analyses show that the identified fracture sets vary their relative abundance and spatial organization with scale, defining a hierarchical network. Fracture length, density, and intensity of each set vary following power-law scaling laws characterized by their own exponents. Comparing the results from each set with those generated from the entire network, we discuss how the obtained scaling laws improve the accuracy of resolving sub-seismic-resolution scale structures, which steer the local-scale permeability of fractured reservoirs. As documented in the field, the identified fracture sets affect the fractured basement permeability differently. Thus, results of multiscale, orientation-dependent statistical analyses, integrated with field analyses of fracture lineaments, can effectively improve the detail and accuracy of permeability prediction of fractured reservoirs. Our results show also how regional geology and analytical biases affect the results of multiscale analyses and how they must be critically assessed before extrapolating the conclusions to any other similar case study of fractured unconventional geofluids reservoirs.

Hosted file

suppinfo_ceccato.docx available at <https://authorea.com/users/529575/articles/597137-scaling-laws-of-fracture-network-properties-in-crystalline-rock-a-powerful-approach-to-the-characterization-of-unconventional-geofluids-reservoirs>

1 **Scaling Laws of Fracture Network Properties in Crystalline Rock: a Powerful Approach to**
2 **the Characterization of Unconventional Geofluids Reservoirs**

3 A. Ceccato, G. Tartaglia, M. Antonellini, G. Viola

4 Corresponding author: Alberto Ceccato, alberto.ceccato@unibo.it

5 Dipartimento di Scienze Biologiche, Geologiche ed Ambientali – BiGeA, Alma Mater Studiorum –

6 Università di Bologna – via Zamboni, 67, 40126 Bologna, Italy

7 **Key points**

- 8 - Multiscale analysis of hierarchical fracture network reveals different scaling properties for
9 individual fracture sets and entire network
- 10 - Power-law scaling laws represent a predictive tool for the quantification of sub-seismic-
11 resolution scale fracture distribution
- 12 - Multiscale, orientation-dependent analyses may improve the accuracy of permeability
13 models of fractured reservoirs

14

15 **Abstract**

16 The multiscale analysis of fracture patterns helps to define the geometric scaling laws and the
17 genetic relationships correlating outcrop- and regional-scale structures in a fracture network. Here
18 we present the results of the multiscale analysis of the geometrical and spatial organization
19 properties of the fracture network affecting the Rolvsnes granodiorite of the crystalline basement of
20 southwestern Norway (Bømlo island). The fracture network shows a spatial distribution described
21 by a fractal dimension $D \approx 1.51$, with fracture lengths distributed following a power-law scaling law
22 (exponent $\alpha = -1.95$). However, orientation-dependent analyses show that the identified fracture
23 sets vary their relative abundance and spatial organization with scale, defining a hierarchical
24 network. Fracture length, density, and intensity of each set vary following power-law scaling laws
25 characterized by their own exponents. Comparing the results from each set with those generated
26 from the entire network, we discuss how the obtained scaling laws improve the accuracy of
27 resolving sub-seismic-resolution scale structures, which steer the local-scale permeability of
28 fractured reservoirs. As documented in the field, the identified fracture sets affect the fractured
29 basement permeability differently. Thus, results of multiscale, orientation-dependent statistical
30 analyses, integrated with field analyses of fracture lineaments, can effectively improve the detail
31 and accuracy of permeability prediction of fractured reservoirs. Our results show also how regional
32 geology and analytical biases affect the results of multiscale analyses and how they must be
33 critically assessed before extrapolating the conclusions to any other similar case study of fractured
34 unconventional geofluids reservoirs.

35

36 **Keywords**

37 Fracture network, Multiscale analysis, Power-law distributions, Fracture length distribution, Sub-
38 seismic-resolution scale.

39 **Plain Language Summary**

40 Fracture and fault zones represent the preferential pathways for fluid flow in igneous and
41 metamorphic rocks, which are commonly characterized by very low intrinsic permeability. In
42 particular, the fractures observed at the outcrop seem to enhance the permeability of such rocks
43 much more than larger-scale fracture and fault zones do. Where fracture networks are well exposed
44 on the Earth surface, they can be mapped at different scales and their spatial distribution and
45 geometrical characteristics quantified. This allows us to retrieve mathematical relationships
46 describing the variation of spatial and geometrical properties across different scales of observation,
47 which can be then adopted to quantify the spatial and geometrical characters of fracture networks at
48 any scale and, in particular, the intensity and geometry of fractures at the outcrop scale. In addition,
49 field analyses taught us that each set of the identified fracture and fault zones affects the
50 permeability of the fractured rock at the outcrop scale in a different manner. The adoption of these
51 mathematical laws, therefore, can aid to quantitatively constrain the variation of permeability of the
52 fractured rock as well.

53

54 **1. Introduction**

55 Fractured crystalline basement units are attracting increasing interest as potential unconventional
56 reservoirs for natural georesources (oil, heat, and water) and as potential disposal or storage sites
57 (nuclear waste, CO₂, H). Crystalline rocks are characterized by very low intrinsic permeability,
58 usually in the order of 10⁻¹⁸ m² (Achtziger-Zupančič et al., 2017; Brace, 1984), such that their
59 capability to transmit and/or store fluids is mainly related to the structural permeability associated
60 with fracture and fault networks developed during brittle deformation (Ceccato, Viola, Antonellini,
61 et al., 2021; Ceccato, Viola, Tartaglia, et al., 2021; Pennacchioni et al., 2016; Schneeberger et al.,
62 2018; Stober & Bucher, 2015). Fracture and fault networks exhibit variable geometrical and spatial
63 characteristics, which need to be assessed and, if possible, quantified to evaluate their effective
64 control on the permeability of the rock mass. Indeed, fractures at different scales may affect and
65 steer fluid flow and reservoir compartmentalization very differently (Le Garzic et al., 2011;
66 Hardebol et al., 2015). For example, long-lived composite fault zones defining regional-scale
67 structures usually control the large-scale compartmentalization of reservoirs (Holdsworth et al.,
68 2019). Being usually identified by means of standard seismic investigations, these structures are
69 generally referred to as Seismic-Resolution Scale (SRS) structures (Tanner et al., 2019). On the
70 other hand, small scale fracture networks, including limited-throw fractures and faults, control the
71 permeability at the outcrop- or borehole-scale (Damsleth et al., 1998; Walsh et al., 1998). These
72 structures are usually not detected and thus imaged by standard seismic investigations, and are
73 therefore referred to as Sub-Seismic-Resolution Scale (SSRS) structures (Tanner et al., 2019). SRS
74 and SSRS structures occurring in a specific region or rock volume are, likely, genetically related
75 and share common characteristics in term of their geometry, spatial organization, and hierarchical
76 relationships (e.g., Holdsworth et al., 2020; McCaffrey et al., 2020).

77 Usually, a multiscale analysis of a fractured medium is adopted to quantify the geometrical
78 characteristics of its fracture network at different scales. Additionally, this approach is necessary to

79 derive mathematical functions, i.e., scaling laws, that describe and constrain the distribution (in
80 terms of density, intensity, relative proportions) of the geometrical features (e.g., length, spacing,
81 throw) of the fracture network across scales (Bossennec et al., 2021; Chabani et al., 2021;
82 Dichiarante et al., 2020; McCaffrey et al., 2020). Scaling laws described by a power-law function
83 can effectively account for the distribution properties of the network at a variety of scales, assuming
84 seamless self-similarity and scale-invariancy of the studied geometrical properties (Bonnet et al.,
85 2001). Nonetheless, self-similarity may actually be limited to only specific scale ranges that are
86 defined by an upper and lower dimensional bound and a characteristic length scale. Also, significant
87 deviations from self-similarity are typical of fracture networks in mechanically layered geological
88 systems, wherein anisotropic mechanical properties, fracture mechanics, and characteristic length
89 scales of the layers may control the development of preferential fracture geometries or spatial
90 organizations (Castaing et al., 1996; Kruhl, 2013; Laubach et al., 2009; Soliva et al., 2006). In those
91 cases, the upscaling of geometrical properties is better performed by adopting other scaling laws
92 such as, for example, negative exponential, log-normal or gamma-law that specifically refer to the
93 identified scale range of pertinence (Bonnet et al., 2001). Conversely, previous authors have
94 suggested that the power-law distribution of both fracture length and spacing is typical of fracture
95 networks within massive crystalline rocks lacking pervasive heterogeneities (Gillespie et al., 1993;
96 McCaffrey et al., 2020; Odling et al., 1999).

97 Here we report the results of the multiscale analysis of lineament maps representing the fracture
98 network deforming the crystalline basement of the island of Bømlo (Western Norway). Fracture
99 network maps were obtained from the manual picking of lineaments on LiDAR digital terrain
100 models, aerial and UAV-drone orthophotos of the exposure area of the Rolvsnes granodiorite (Fig.
101 1). The fractured (and weathered) crystalline basement exposed in Bømlo is thought to represent the
102 on-shore analogue of an offshore unconventional oil reservoir hosted in the Utsira High in the North
103 Sea (Fredin et al., 2017; Riber et al., 2015; Trice et al., 2019). The fracture network within the

104 Rolvsnes granodiorite represents a good example of fracture network developed during a prolonged
105 brittle tectonic history within massive, isotropic granitoid rocks. The in-situ analysis and
106 characterization of representative constituents of this fracture and fault zones network, e.g., the
107 Goddo Fault Zone (GFZ, Fig. 1), has previously allowed us to reconstruct in detail the timing of
108 deformation and to quantify its fracture geometry and petrophysical properties (Ceccato, Viola,
109 Antonellini, et al., 2021; Ceccato, Viola, Tartaglia, et al., 2021; Scheiber & Viola, 2018; Viola et
110 al., 2016). This notwithstanding, the larger-scale geometry and organization of these fracture and
111 fault network remain poorly constrained and need quantification.

112 Our statistical analysis of the fracture network properties was conducted at different scales of
113 observation aiming to identify the scaling relationships (if any) for each analyzed property. Fracture
114 network properties include: (i) fractal dimension D ; (ii) lineament orientation; (iii) cumulative
115 length distribution of lineaments at each scale and for each orientation set; (iv) intensity/density
116 scaling for the whole lineament network and for each orientation set. The ultimate goal is to
117 characterize in detail the scaling relationships (and understand their limitations) for the geometrical
118 properties of the Rolvsnes fracture network as a possible analogue for the fracture network
119 documented in the offshore Utsira High unconventional oil reservoir hosted in a fractured and
120 weathered crystalline basement (Fredin et al., 2017; Trice et al., 2019). These analyses represent a
121 powerful tool for the identification of SSRS structures, the quantification of their heterogeneous
122 distribution and, accordingly, the heterogeneous distribution of permeability of the fractured
123 crystalline basement at different scales. The implications of the adoption of general scaling laws on
124 the upscaling/downscaling of fracture network properties, as well as the possible analytical biases
125 and sources of errors in the analytical approach, are finally evaluated and discussed.

126 **2. Geological setting**

127 The crystalline basement of Bømlo belongs to the Upper Allochthon units of the Caledonian orogen
128 (Gee et al., 2008). Our lineament maps represent the fracture pattern affecting the Rolvsnes

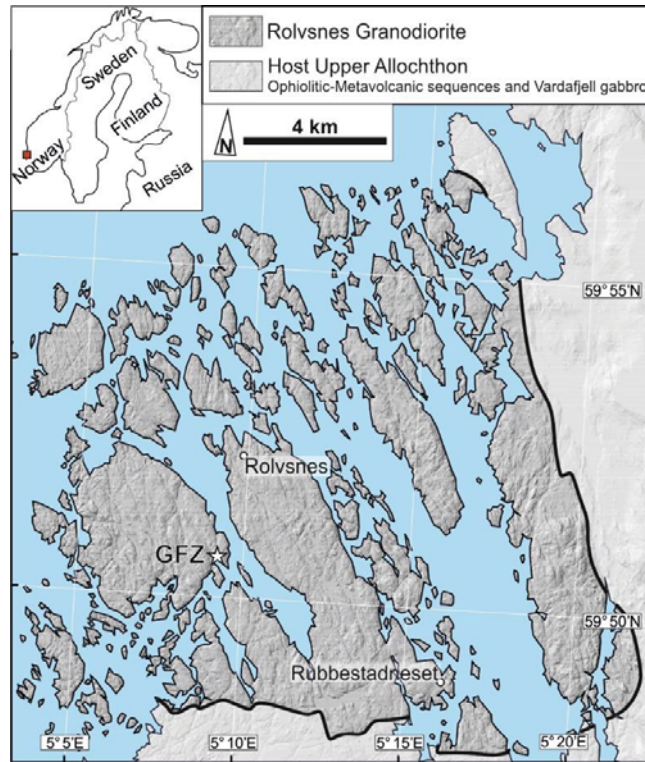
129 granodiorite, a pre-Scandian (466 ± 3 Ma; zircon U-Pb dating) granitoid pluton hosted in the Upper
130 Allochthon metamorphic units (Scheiber et al., 2016) (Fig. 1). The Rolvsnes granodiorite recorded a
131 prolonged and multi-phase brittle deformation history (Scheiber et al., 2016; Scheiber & Viola,
132 2018), only briefly summarized in the following, while the reader is referred to the cited literature
133 for a more detailed and comprehensive description of the tectonic history of the area. Overall, the
134 whole tectonic history of the area is the expression of three main deformation episodes (Bell et al.,
135 2014; Fossen et al., 2016, 2021): (1) Caledonian convergence and continental collision from the
136 Mid-Ordovician to the Silurian; (2) extensional tectonics related to the late-Scandian orogenic
137 collapse during the Devonian, and (3) prolonged and multi-phase extensional tectonics related to the
138 North Sea rifting from the Permian to the Cretaceous. During this tectonic evolution, the pre-
139 Scandian Rolvsnes granodiorite did not record penetrative ductile strain and was instead affected by
140 pervasive brittle deformation. Each tectonic stage has been related to a characteristic set of fracture
141 and fault zones that dissect Bømlo (Scheiber & Viola, 2018): (1) NNW- and WNW-striking
142 conjugate strike-slip faults developed coevally with ENE-WSW-striking reverse faults during
143 Caledonian convergence; (2) the same structures were reactivated with opposite kinematics during
144 the early stages of late-Scandian orogenic collapse; (3) NW- and NNW-striking normal faults
145 ascribable to the regional Permian-to-Jurassic rifting phase of the North Sea, which partially
146 reactivated earlier, inherited structures. During the latest rifting stages of the North Sea, in the Early
147 Cretaceous, new and N- to NNE-striking fracture corridors and normal faults overprinted the
148 previously formed fracture pattern. Indeed, our lineament maps depict efficiently the complex and
149 multiscale network of fractures and fault zones affecting the crystalline basement of Bømlo, which
150 have been repeatedly reactivated during the prolonged rifting history of the North Sea (Ceccato,
151 Viola, Tartaglia, et al., 2021; Scheiber & Viola, 2018; Viola et al., 2016).

152 A key structure for the detailed analysis of the timing of deformation, the geometry of the
153 deformation structures, and the effects of deformation on the petrophysical properties of the

154 crystalline basement of Bømlo, is the Goddo Fault Zone (Fig. 1), (Ceccato, Viola, Antonellini, et
155 al., 2021; Ceccato, Viola, Tartaglia, et al., 2021; Scheiber & Viola, 2018; Viola et al., 2016). The
156 Goddo Fault Zone is an east-dipping normal fault that accommodated multiple slip increments
157 during the prolonged Permian-to-Cretaceous rifting of the North Sea, recording several stages of
158 reactivation, during which a complex network of brittle structural facies developed in the fault core
159 (*sensu* Tartaglia et al., 2020). Structures like the Goddo Fault Zone actually controlled the
160 permeability and fluid flow evolution from rifting to current times of the crystalline basement
161 (Ceccato, Viola, Antonellini, et al., 2021; Ceccato, Viola, Tartaglia, et al., 2021; Viola et al., 2016).

162 Similarly to Bømlo, a complex fracture and fault network developed in the crystalline basement of
163 the Utsira High, of which the Rolvsnes granodiorite is interpreted as the onshore analogue (Fredin
164 et al., 2017; Trice et al., 2019). The Utsira High crystalline basement is composed of (likely
165 multiple) pre-Scandian igneous intrusions of similar age and composition to the Rolvsnes
166 granodiorite (Lundmark et al., 2014; Slagstad et al., 2011). The fracture network in the Utsira High
167 developed under tectonic conditions similar to those of the Bømlo crystalline basement, but with
168 several significant differences mainly related to the structural position of the two crystalline
169 basements within the North Sea rifting region (Bell et al., 2014).

170



171

172 **Figure 1.**

173 Simplified geological map of the Bømlo Island reporting the area where the Rolvnes granodiorite
174 crops out overlaying the Digital Terrain Model obtained from high-resolution (1 m) LiDAR survey.

175

176

177 3. Materials and Methods

178 The fracture/lineament maps (Fig. 2a) used for the multiscale analyses presented here have been
179 generated in ArcGIS 10.8 by manually picking the same digital terrain model (DTM) of selected
180 areas of Bømlo at different scales of observation. DTM's from high-resolution (1 m) airborne Light
181 Detection and Ranging (LiDAR) surveys (Fig. 1) have been used for the manual picking of fracture
182 lineaments at the 1:5,000; 1:25,000 and 1:100,000 scales. The details of LiDAR data acquisition
183 and DTMs elaboration can be found in Scheiber et al. (2015). In addition, the dataset of fracture
184 lineaments interpreted from LiDAR DTM at the 1:5,000 scale was integrated with the interpretation
185 of aerial orthophotos from the Bing Maps database (<https://www.bing.com/maps>). Bing aerial
186 imagery was also adopted to distinguish between natural and man-made linear structures and to
187 check for artefacts and potential misinterpretation of linear features on LiDAR-derived DTMs in the
188 absence of systematic ground truthing. The outcrop-scale lineament picking was performed on
189 digital orthophotos of a key Goddo Fault Zone outcrop (Figs. 1, 3a) as obtained from the
190 elaboration of the imagery collected via UAV-drone surveys through Structure-from-Motion (SfM)
191 algorithm. Details on this acquisition and its elaboration methods can be found in Ceccato, Viola,
192 Antonellini, et al. (2021). Topographic lineaments were traced as single, linear segments (not
193 polylines) interpreting their topographic expression on DTMs. This interpretation technique
194 introduces two major analytical biases on the obtained lineament maps: 1) the interpreted length
195 may only partially represent the entire lineament (which may be covered by deposits or be
196 differently expressed in the topography, thus being not visible in its entire length, e.g., Cao & Lei,
197 2018); 2) as a consequence, abutting relationships, intersections between lineaments and lineament
198 network topology and connectivity remain highly speculative and susceptible to subjective biases
199 (Andrews et al., 2019). The orientation of mapped lineaments, expressed as azimuth angle from the
200 geographic north, was calculated in ArcGIS 10.8 using the freely available tool Easy Calculate 10
201 (https://www.ian-ko.com/free/free_arcgis.htm) and the Orientation Analysis Tools
202 (<https://is.muni.cz/www/lenka.koc/prvnistrana.html>). Rose diagrams plotting lineament azimuths

203 were produced with the MARD 1.0 software (Munro & Blenkinsop, 2012). Lineament density P_{20}
204 (m^{-2}) and intensity P_{21} (m/m^2) (Dershowitz & Herda, 1992) were calculated as the ratio between the
205 total number of lineaments and total length of lineaments, respectively, over the total area of the
206 land exposure in each lineament map.

207 *3.1. Fractal dimension – Box-counting method*

208 The fractal dimension of each lineament map at different scales was computed with the box-
209 counting method (Bonnet et al., 2001; Gillespie et al., 1993), adopting the freely available function
210 `boxcount.m` in MATLAB R2019b ([http://www.fast.u-
211 psud.fr/~moisy/ml/boxcount/html/demo.html](http://www.fast.u-psud.fr/~moisy/ml/boxcount/html/demo.html)). The box-counting method consists in subdividing
212 the analyzed image in progressively smaller square boxes of side b and counting how many of them
213 contain a segment of the analyzed lineament network. Plotting the number n of boxes containing at
214 least one lineament against the side length b on a log-log diagram should yield a straight curve,
215 whose slope defines a power-law function with D as the fractal exponent (Bonnet et al., 2001). The
216 fractal dimension obtained from the box-counting method quantifies the scaling properties of the
217 spatial occupancy of the fracture network (Bonnet et al., 2001).

218 *3.2. Cumulative length distribution analyses*

219 Length data of lineaments extracted from lineament maps have been organized as cumulative
220 distributions and plotted in log-log diagrams of the length L of lineaments on the X-axis versus the
221 cumulative number N of lineaments with length $l > L$ (Fig. 2b-c). The cumulative length
222 distributions were then normalized by the area of the land surface reported on each map over which
223 the lineaments were picked. Cumulative length distributions have then been analyzed by means of
224 the Maximum Likelihood Estimation (MLE) and Kolmogorov-Smirnov (KS) statistical tests to
225 retrieve the best fitting mathematical function (Dichiarante et al., 2020; Kolyukhin & Torabi, 2013;
226 Rizzo et al., 2017). The mathematical functions considered were negative exponential, power-law
227 and log-normal (Fig. 2b). The advantage of adopting MLE-KS statistical tests derives from the

228 possibility to also retrieve the function parameters (namely the exponent λ for the exponential, the
229 exponent α for the power-law and the mean μ and standard deviation σ for the log-normal
230 functions) in addition to the mathematical function best approximating the observed cumulative
231 length distributions. A dedicated MATLAB script implementing the freely available functions
232 provided in the latest version of FracPaQ (Healy et al., 2017; Rizzo et al., 2017) was used to this
233 purpose. The results of the MLE-KS analyses are presented as “checkerboard” diagrams, following
234 the method proposed by Dichiarante et al. (2020) (Fig. 2d). Such diagrams allow to image the
235 results of the MLE-KS analyses performed on the selected portions of the cumulative distribution,
236 i.e., the best fitting mathematical function for variable subdomains of the cumulative distribution. A
237 subdomain is defined as a segment of the cumulative distribution curve bounded by a lower and
238 upper cut value (Fig. 2c-d). The upper cut value represents the distance, expressed in terms of
239 percentage of the total number of elements contained in the cumulative distribution, from the
240 shortest observed length. The lower cut value represents the distance, in terms of percentage of the
241 total number of elements contained in the cumulative distribution, from the longest observed length.
242 On the checkerboard diagrams, the lower cut values are plotted versus the upper cut values (Fig.
243 2d). Each point of the checkboard therefore represents a specific percentage range of the total
244 cumulative distribution between the upper and lower cut limits over which the MLE-KS tests have
245 been run. The plotted symbol represents the mathematical function among those considered (power-
246 law, exponential, log-normal) for which the MLE-KS tests yielded the highest fitting score, whereas
247 the symbol is color-coded according to the retrieved value of the fitting scores (namely HP and PP
248 parameters, see Rizzo et al., 2017; Dichiarante et al., 2020). This analytical approach allows to
249 determine the mathematical function that best fits the truncated cumulative distribution and to
250 evaluate the effect of truncation and censoring biases (Fig. 2c-d). The MLE-KS analyses were
251 performed for the cumulative length distribution of the entire set of lineaments contained in each
252 map at each scale of observation (1:100; 1:5,000; 1:25,000; 1:100,000) and for the cumulative
253 distributions of lineaments classified according to their orientation for each scale. In addition, the

254 cumulative length distributions representing the entire population of each lineament map and each
255 lineament set at different scales of observation have been plotted on a cumulative log-log diagram
256 in order to evaluate the “general” relationship that may link cumulative distributions observed at
257 different scales.

258 *3.3.Spatial distribution analysis*

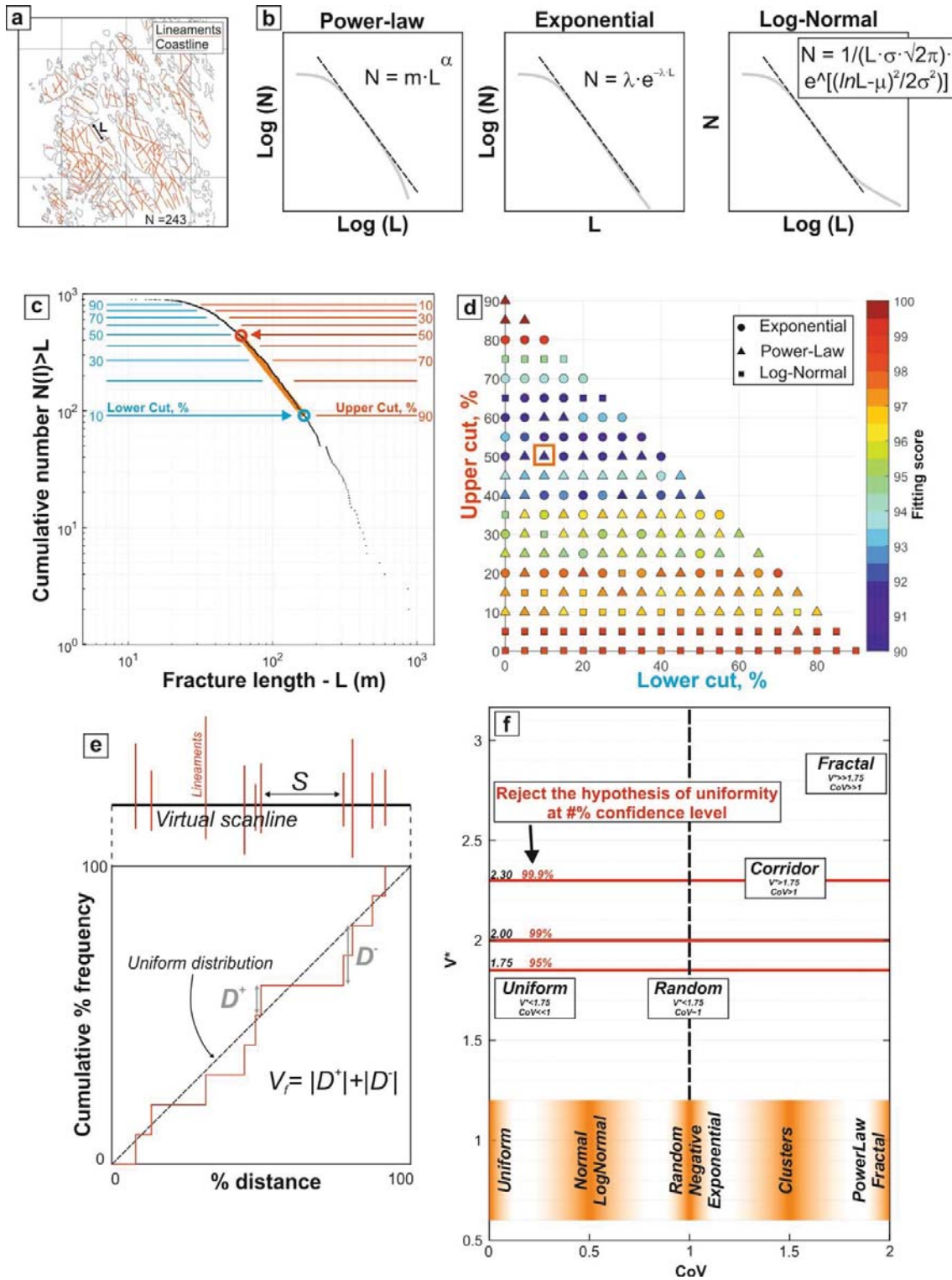
259 The spatial distribution of lineaments has been quantified by following the approach by Sanderson
260 and Peacock (2019). We analyzed the statistics of spacing between lineaments collected along
261 virtual scanlines computed with the NetworkGT toolkit in QGis 3.12.2 (Nyberg et al., 2018) (e.g.,
262 Fig. 2e). The lineaments were classified and grouped into orientation sets according to the results of
263 the orientation analysis. A grid of equally-spaced virtual scanlines oriented perpendicular to the
264 selected lineament set orientation was draw upon the imported lineament map with NetworkGT
265 (e.g., Fig. 2e). With NetworkGT we collected and analyzed the intersections between each virtual
266 scanline and the lineaments reported on the map. For each scanline, we analyzed the statistics
267 (average value, standard deviation – 2σ , minimum and maximum values) of several parameters
268 (Fig. 2e): (i) spacing (S) between two intersected lineaments; (ii) Coefficient of Variation (CoV) of
269 the spacing, defined as the ratio between the standard deviation of spacing along a scanline and its
270 average ($\text{CoV} = \sigma S / \langle S \rangle$) (Gillespie et al., 1993); (iii) coefficient of heterogeneity (V_f) and its
271 statistical significance (V^*) according to Sanderson and Peacock (2019). The Coefficient of
272 Variation (CoV) of spacing is commonly adopted to assess the spatial organization (clustering vs.
273 uniform distribution) of fractures along linear scanlines (e.g. Gillespie et al., 1993). In particular,
274 CoV values > 1 are usually related to the occurrence of clustered fracture distributions; $\text{CoV} = 1$
275 should represent a (negative) exponential-random distribution of spacing intervals, and $\text{CoV} < 1$ is
276 usually related to log-normal (uniform) spacing distributions (Gillespie et al., 1993; McCaffrey et
277 al., 2020; Odling et al., 1999). The spacing heterogeneity, i.e., the deviation of the spacing
278 distribution along a scanline from a uniform distribution, is quantified by the V_f and V^*

279 coefficients, as computed by adopting the method by Kuiper (Sanderson & Peacock, 2019). The
 280 coefficient of heterogeneity V_f quantifies the deviation from a theoretical uniform distribution of the
 281 observed spacing distribution along a given scanline expressed as the sum of the moduli of the
 282 positive and negative deviations (see Sanderson and Peacock, 2019; Fig. 2e). The coefficient V^*
 283 quantifies the statistical significance of the heterogeneity factor V_f :

$$284 \quad V^* = V_f \left(\sqrt{N} + 0.155 + \frac{0.24}{\sqrt{N}} \right);$$

285 where N represents the number of intersected fractures along the scanline. As reported in Sanderson
 286 & Peacock (2019), “Stephen (1970) showed that if $V^* > 1.75$, 2.0 and 2.3, one can reject the null
 287 hypothesis of uniformity at the 95%, 99% and 99.9% levels, respectively”. Thus, the coefficient V^*
 288 can be used to quantify the probability that a certain spacing distribution is uniform or not. We have
 289 performed a combined analysis of CoV and V^* because of the limited amount of intersections
 290 recorded by each virtual scanline ($\ll 30$ fractures per scanline) in our maps. For the same reason,
 291 more advanced and up-to-date analyses of the spacing variability (e.g., Marrett et al., 2018;
 292 Sanderson & Peacock, 2019; Bistacchi et al., 2020) were not possible. We present the results of this
 293 analysis in CoV- V^* diagrams (e.g., Fig. 2f), wherein the coefficient of variation of spacing is
 294 plotted against the statistical significance of the spacing heterogeneity computed with the Kuiper’s
 295 method. The statistical distribution of the CoV and V^* values characterizes the general spatial
 296 organization of each orientation set of lineaments (Sanderson & Peacock, 2019). Plotting the
 297 statistical distribution (box-and-whiskers) of the values of CoV vs. V^* , we can qualitatively
 298 evaluate if, statistically, a set of fractures tends to present a random or organized spatial distribution.
 299 With this method, four main spatial organization types can be distinguished (Fig. 2f): (i) Uniform
 300 distribution, characterized by $\text{CoV} \ll 1$ and $V^* < 1.75$; (ii) random distribution, characterized by
 301 $\text{CoV} \approx 1$, $V^* < 1.75$; (iii) Corridor-Clustered distribution, characterized by $\text{CoV} > 1$ and $V^* > 1.75$ -
 302 2.00; (iv) Fractal distribution, characterized by $\text{CoV} \gg 1$ and $V^* \gg 1.75$ -2.00. Scanlines with

303 more than 10, 5 and 3 intersections were considered for the analysis of lineament maps at 1:5,000,
 304 1:25,000, 1:100,000, respectively.



305

306 **Figure 2.**

307 Explanatory figure supporting the Method section. (a) Example of lineament map retrieved from the
308 analysis of small scale DTMs. (b) Schematic representation of power-law, negative exponential and
309 log-normal distributions, each of which defines a linear relationship between length L and
310 cumulative number N on a log-log, linear-log or log-linear diagram, respectively. (c) Example of
311 cumulative length distribution, plotted on a log-log diagram, obtained from the analysis of
312 lineament maps explaining graphically what the upper cut and lower cut values are. The blue and
313 red circles represent the upper and lower cut values related to the checkerboard in (d). The orange
314 segment represents the sub-domain of the cumulative distribution, included between the upper cut
315 and lower cut bounds, fitted by the power-law relation identified by MLE-KS tests. (c) Example of
316 checkerboard diagram. Each symbol (circle, triangle, square) represents a different fitting function,
317 and each symbol is color-coded according to the fitting score yielded by the MLE-KS test for the
318 portion of the cumulative distribution delimited by upper and lower cut values (plotted on the Y-
319 and X-axis, respectively). The orange square represents the results of the MLE-KS tests performed
320 on the distribution subdomain shown in (c). (e) Schematic representation of a virtual scanline and
321 the related diagram showing the difference (D values) between the observed lineament distribution
322 and a theoretical uniform (constant) distribution of spacings. (f) CoV- V^* diagram showing the
323 expected ranges for uniform, random, clustered and fractal spacing distributions.

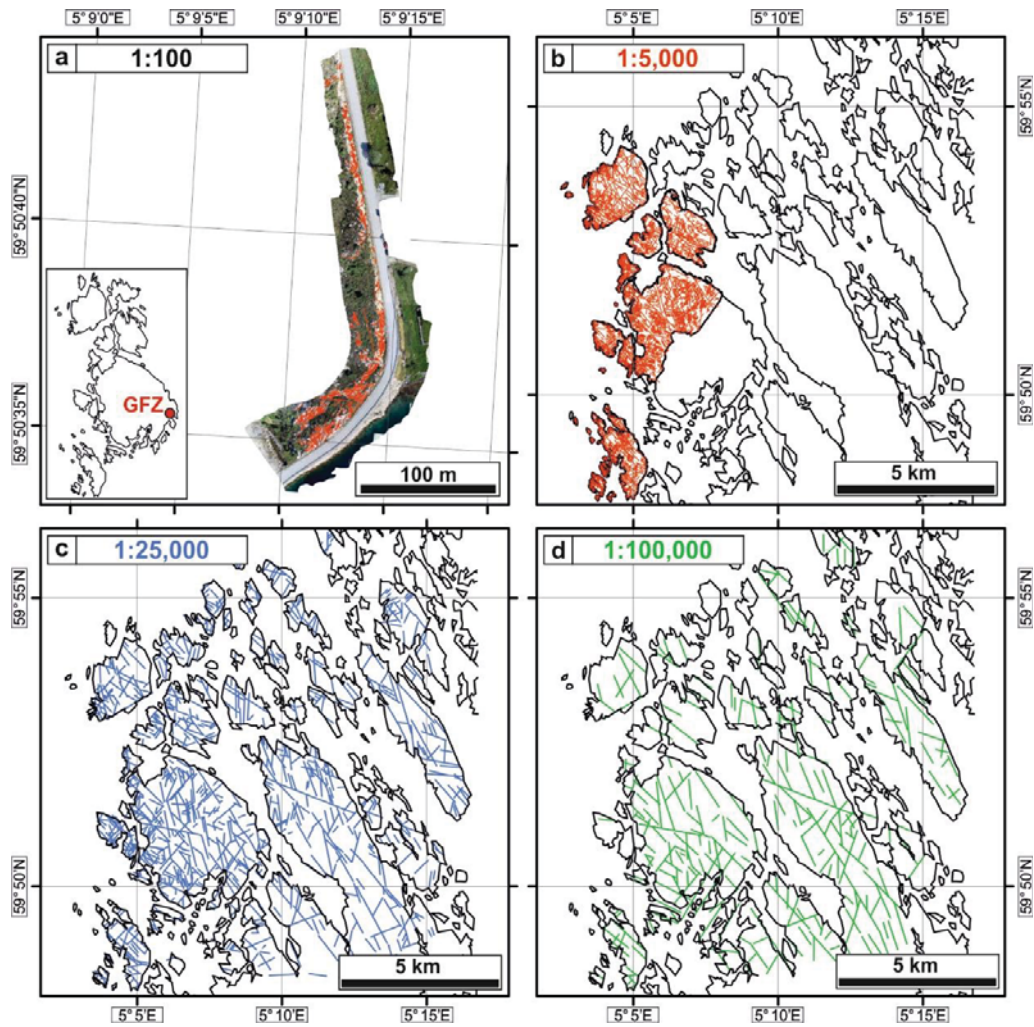
324

325

326 4. Results

327 4.1. Lineament maps description

328 The manual picking of topographic lineaments on different digital representations of Bømlo led to
329 the production of lineament maps with the spatial distribution and organization of topographic
330 lineaments at different scales (Fig. 3). The orthophotos retrieved from UAV-drone surveys and the
331 related lineament map (Fig. 3a) help characterize the main outcrop of the Goddo Fault Zone along
332 the eastern shoreline of the island of Goddo (Ceccato, Viola, Antonellini, et al., 2021; Ceccato,
333 Viola, Tartaglia, et al., 2021; Viola et al., 2016). Even though the number of lineaments interpreted
334 from UAV-drone imagery is statistically significant ($n=930$), the N-S- trending outcrop exposure,
335 its 3D topography and the location of the exposed area along a major fault zone question whether
336 the obtained results may be truly representative of the larger-scale fracture network. Lineament
337 mapping on LiDAR DTM and aerial imagery at 1:5,000 scale (Fig. 3b) was thus performed on the
338 best exposed areas along the coastline of the Goddo Island and the nearby smaller islands. The
339 resulting lineament map covers more than 17 km^2 and includes $n=3,835$ interpreted lineaments.
340 Furthermore, we generated additional lineament maps from the interpretation of the LiDAR DTM at
341 the 1:25,000 and 1:100,000 scales, which cover the same area (83 km^2 ; Fig. 3c-d). The 1:25,000
342 lineament map contains $n=894$ lineaments, whereas the 1:100,000 map contains $n=249$ lineaments.



343

344 **Figure 3.**

345 Lineament Maps retrieved from the manual lineament picking on outcrop orthophotos (a) and DTM

346 from LiDAR surveys (b-c-d).

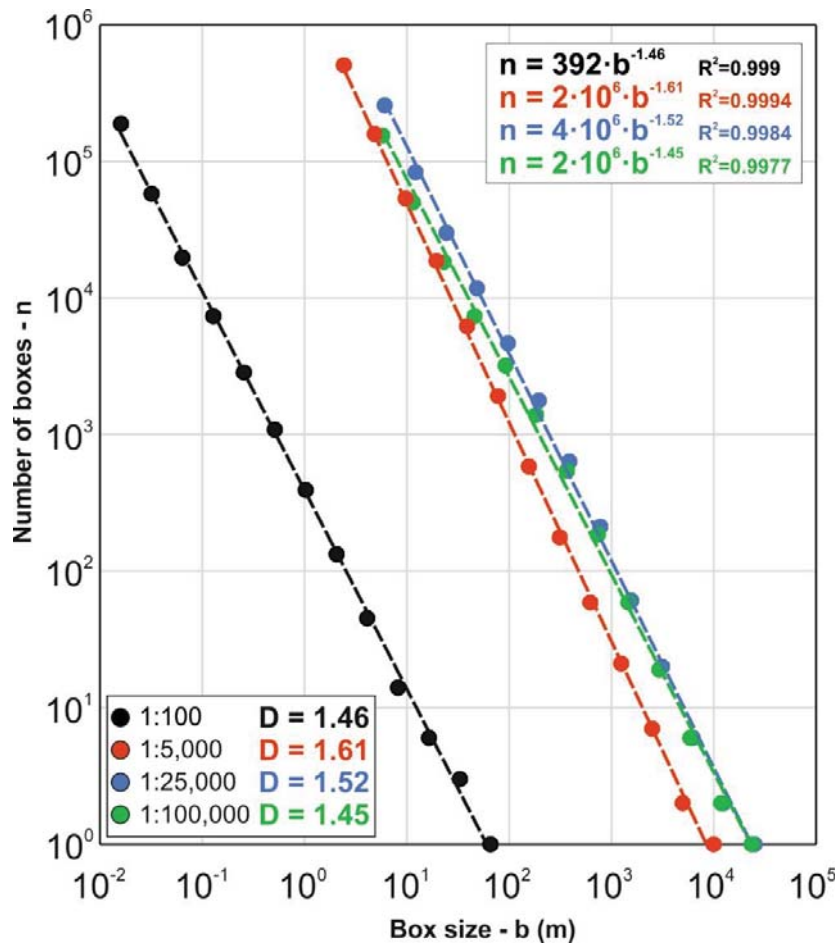
347

348

349

350 *4.2. Fractal dimension*

351 The fractal dimension of the lineament maps at all scales was evaluated by applying the box-
 352 counting method (Bonnet et al., 2001; Gillespie et al., 1993) (Fig. 3). The number of filled boxes
 353 decreases with increasing box size following a power-law relationship (Fig. 4). The power-law
 354 exponents (the fractal exponent D) retrieved from the box counting analyses of the lineament maps
 355 at different scales ranges between 1.45 and 1.61 (Fig. 4). On average, the fracture network is
 356 characterized by a fractal dimension $D = 1.51 \pm 0.14$ (2σ).



357

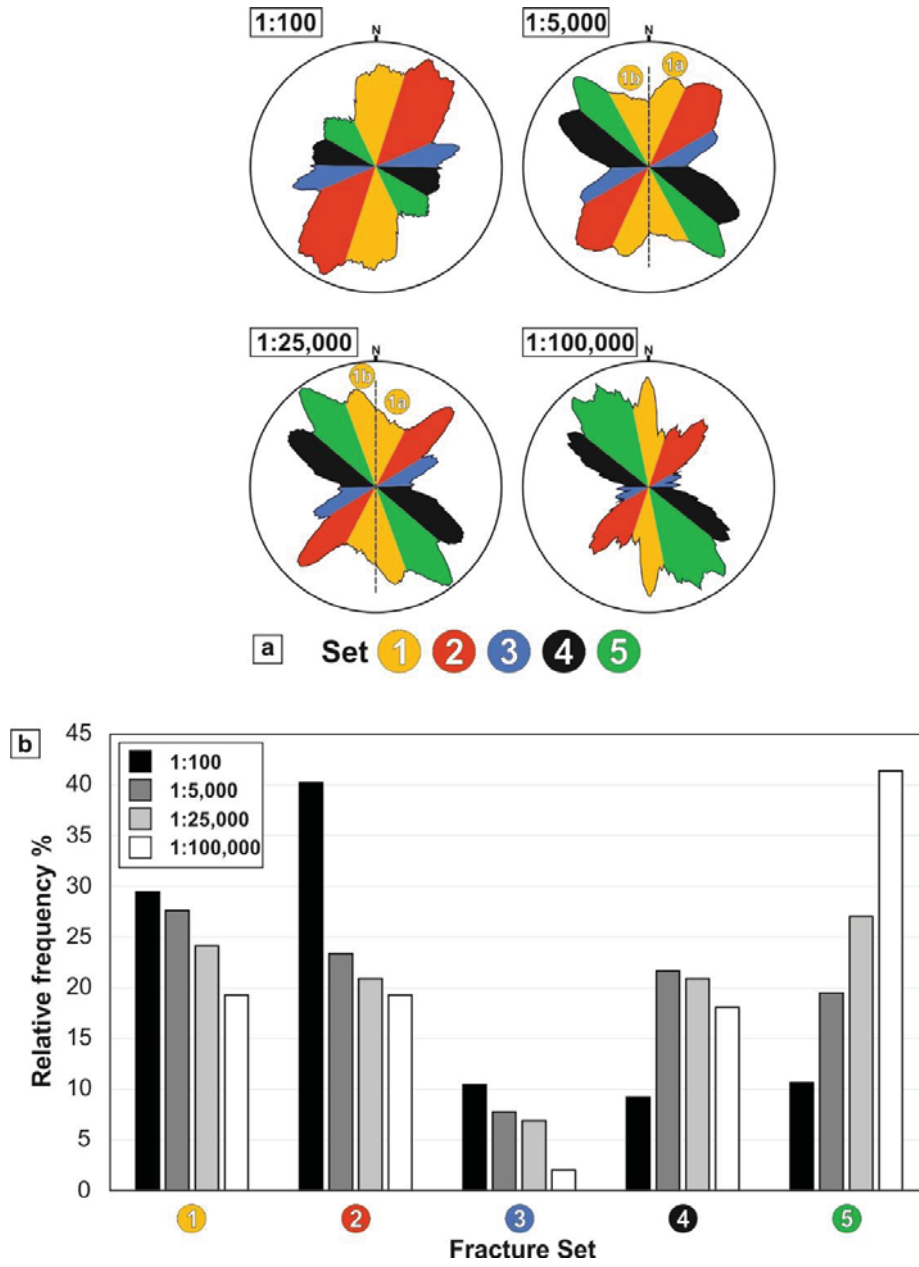
358 **Figure 4.**

359 Results of the box-counting method applied to the lineament maps of Fig. 3.

360

361 4.3. *Orientation*

362 The comparison of the rose diagrams at different scales of observation makes it possible to define
363 some dominant orientation trends in the study area (Fig. 5a-b). The five main identified orientation
364 trends are (Fig. 5a, Supplement S1, Table 1): (a) a N-S-striking Set 1; (b) a NE-SW-striking Set 2;
365 (c) a ENE-WSW-striking Set 3; (d) a ESE-WNW-striking Set 4, and (e) a SE-NW-striking Set 5.
366 These sets display a significant variation of their relative abundance across the scales. At the
367 smallest scale of observation (1:100,000), Set 5 is dominant, whereas at the largest observation
368 scale (1:100), Sets 1 and 2 are dominant (Fig. 5b). At intermediate scales (1:5,000; 1:25,000), all
369 sets are equally represented (Table 1). Set 3 is the least represented, occurring in only small
370 percentages (<10%) at all scales (Table 1). Sets 2 to 5 have a constant average orientation across all
371 scales but Set 1 lineaments have a variable average orientation with scale. Average N-S-striking
372 orientations are dominant at the smallest and largest scales of observation. At the intermediate scale,
373 Set 1 presents either a NNW- (scale 1:5,000) or a NNE dominant strike (scale 1:25,000) (Fig. 5a).
374 Therefore, we have subdivided Set 1 into Set 1a, including NNE-SSW-striking lineaments, and Set
375 1b, including N-S- to NNW-SSE-striking lineaments. This subdivision will be mainly adopted for
376 the analysis of the spatial organization of the lineaments.



377

378 **Figure 5.**

379 Rose diagrams (a) and histograms of the relative frequencies (b) of the identified orientation sets at
 380 different scales of observation.

381

382

	Set	Azimuth (°)	N	Relative frequency (%)	Avg P ₂₀ (m ⁻²)	Total Length (m)	Avg P ₂₁ (m/m ²)
Scale		1:100					
Area (m²)	1	0-17; 156-180	274	29.46	0.1288	490.1	0.2304
2127	2	19-67	374	40.22	0.1758	771.86	0.3629
	3	68-91	97	10.43	0.0456	156.25	0.0735
	4	92-120	86	9.25	0.0404	134.12	0.0631
	5	121-155	99	10.65	0.0465	175.3	0.0824
	Total		930		0.4372	1727.63	0.8122
Scale		1:5,000					
Area (m²)	1	0-28; 154-180	1059	27.61	6.16754E-05	103655.02	0.0060
17170533	2	29-60	896	23.36	5.21824E-05	76172.72	0.0044
	3	61-88	299	7.80	1.74136E-05	23934.34	0.0014
	4	89-130	832	21.69	4.84551E-05	80080.14	0.0047
	5	131-153	749	19.53	4.36212E-05	90759.34	0.0053
	Total		3835		0.000223348	374601.56	0.0218
Scale		1:25,000					
Area (m²)	1	0-25; 162-180	216	24.16	2.60239E-06	93912.71	0.0011
83000724	2	26-59	187	20.92	2.25299E-06	60252.45	0.0007
	3	60-90	62	6.94	7.46981E-07	20544.88	0.0002
	4	91-131	187	20.92	2.25299E-06	74024.49	0.0009
	5	131-161	242	27.07	2.91564E-06	113476.26	0.0014
	Total		894		1.0771E-05	362210.79	0.0044
Scale		1:100,000					
Area (m²)	1	0-19; 171-180	48	19.28	5.78308E-07	35972.83	0.0004
83000724	2	20-60	48	19.28	5.78308E-07	38877.02	0.0005
	3	61-90	5	2.01	6.02404E-08	4354.5	0.0001
	4	91-130	45	18.07	5.42164E-07	36742.25	0.0004
	5	131-171	103	41.37	1.24095E-06	106590.06	0.0013
	Total		249		2.99997E-06	222536.66	0.0027

383

384 **Table 1.**

385 Table presenting the orientation data for the identified lineament sets for each scale of observation.

386

387

388 *4.4. Cumulative length distributions*

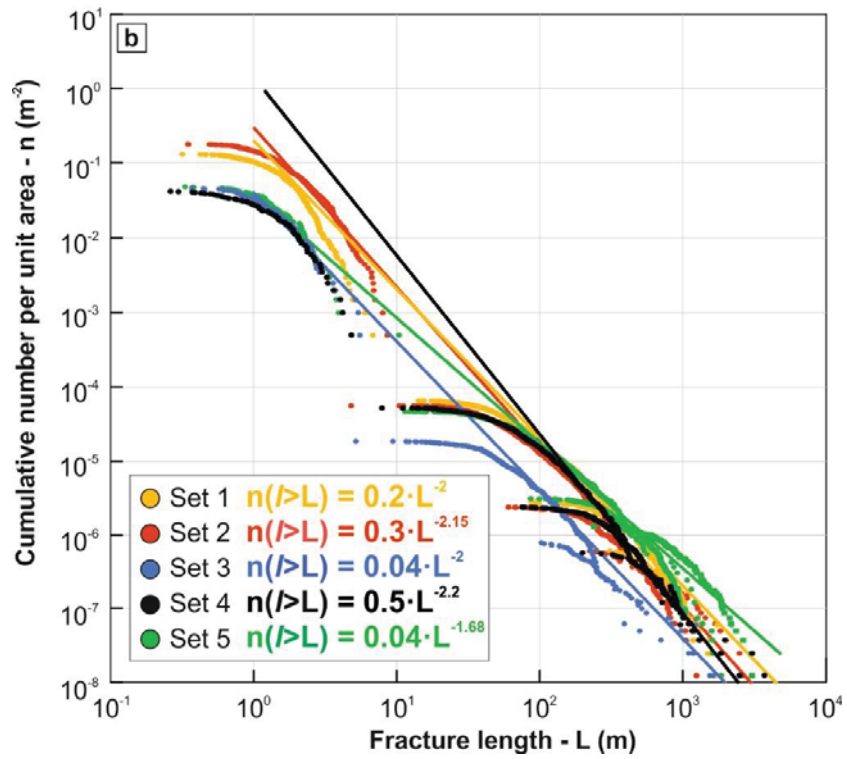
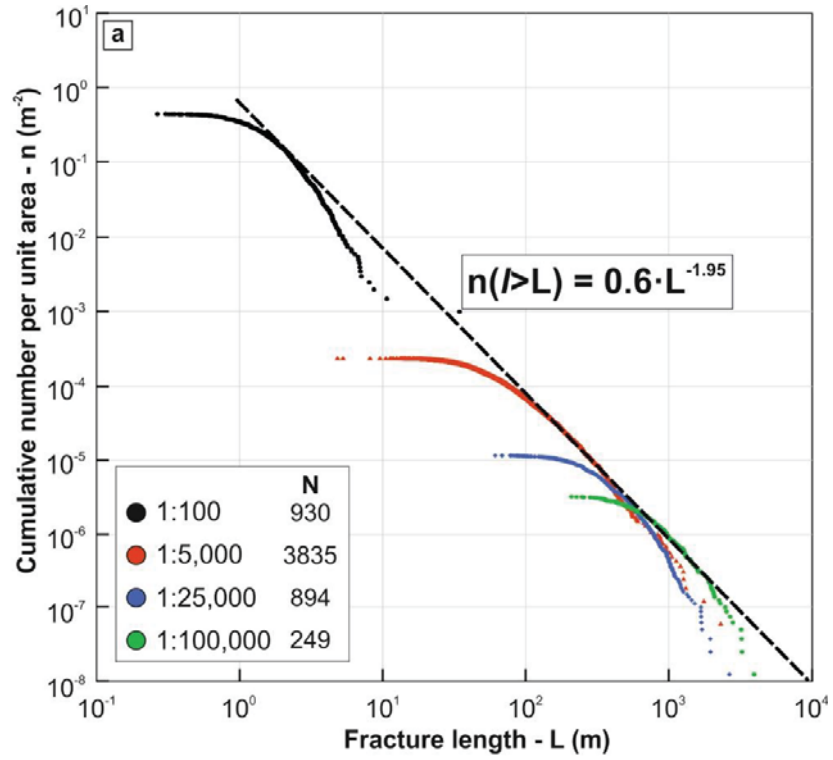
389 We have analyzed the length probability distribution function of (i) all lineaments included in each
390 lineament map at different scales (Fig. 6a) and (ii) each lineament set at different scales (Fig. 6b).

391 We have performed the MLE-KS statistical tests for each set at different scales and the cumulative
392 distribution at each scale to define the best fitting function for each probability distribution (Table
393 2). The results of MLE-KS tests are reported and summarized in Table 2; the checkerboards
394 diagrams are reported in the supplementary material (Fig. Supplement S2).

395 We present in Table 2 the range of upper cut values for which each function fits best: the upper cut
396 values quantify the “truncation” of the cumulative distribution at short lengths, and this has been
397 demonstrated to deeply affect the results of MLE-KS tests (Dichiarante et al., 2020). Where
398 possible, we have also considered the minimum number of fractures to retrieve a statistically
399 significant distribution (number of lineaments >200; red lines in Fig. Supplement S2) (Bonnet et al.,
400 2001).

401 The results of the MLE-KS tests suggest that a log-normal function best approximates the entire
402 probability distribution in all considered cases (Fig. Supplement S2; Table 2). Variably truncated
403 distributions are best approximated by either negative exponential or power-law functions (Table
404 2). In particular, the truncated length probability distributions for both single sets and the entire
405 lineament network mapped at the large scale (1:100) of the GNF outcrop are best represented by
406 negative exponential functions, with λ ranging between 0.65 and 1.25. Truncated distributions
407 retrieved from lineament maps at 1:5,000 are best fitted, in most cases, by power-law functions with
408 a minimum exponent α of 2.2. The truncated distributions of Sets 3 and 4 mapped at 1:5,000 can be
409 described by both negative exponential and power-law functions. Truncated length distributions for
410 lineaments mapped at 1:25,000 and 1:100,000 scale are well approximated by negative exponential
411 functions, with an average λ of 0.004 and 0.0017, respectively (Table 2).

412 Figure 6a reports the cumulative length distributions for the entire set of lineament maps normalized
413 to the area of investigation at each scale of observation. Even though each cumulative distribution is
414 best approximated by either power-law or exponential (or log-normal) functions (Table 2), all the
415 plotted normalized cumulative distributions seem to obey a general power-law relationship valid
416 over five orders of magnitude (1 m to 10,000 m). The power-law exponent α is -1.95 (Fig. 6a).
417 Figure 6b reports the cumulative length distributions for each set of lineaments mapped at different
418 scales and normalized for the area of investigation. Also in this case, all the plotted distributions
419 obey a general power law scaling with a characteristic exponent α for each set of lineaments (Fig.
420 6b, Supplement S3). The exponent α ranges between -1.68 and -2.2. The cumulative distributions
421 for Set 4 lineaments mapped at the 1:5,000, 1:25,000 and 1:100,000 scale are approximated well by
422 a general power-law function with an average exponent $\alpha = -2.2$. Set 4 lineaments at the 1:100
423 scale, however, do not plot along this general power-law trend (Fig. 6b, Supplement S3).



425 **Figure 6.**

426 (a) Log-log diagram showing the cumulative length distribution for the whole lineament maps
427 reported in Fig. 3, normalized by the investigated area. (b) Log-log diagram showing the cumulative
428 length distribution for each orientation set.

429

430

431

432 **Table 2.**

433 Summary table of the results of MLE-KS statistical tests on distribution fitting. The results showing
 434 the highest fitting score from MLE-KS tests are indicated by a grey background.

Scale	Set	n	Length min (m)	Length max (m)	Avg Length (m)	Exponential			Power-law			Log-Normal				
						Fitting Score	Range (UC %)	λ	Xmin (m)	Fitting Score	Range (UC %)	α	Xmin (m)	Fitting Score	Range (UC %)	μ
1:100	1	274	0.3	6.9	1.8	>90	40-90	1.05-1.25	>1.4	-	-	-	>90	0.35	0.45-0.75	0.52-0.37
	2	374	0.3	8.7	2.1	>90	>10	0.65-0.79	>0.9	-	-	-	>90	0.5	0.55-0.65	0.55-0.57
	3	95	0.4	5.6	1.6	>90	10-65	0.95-1.05	0.8-1.8	>90	70-85	3.8-5	>90	0.5	0.35-0.45	0.5-0.55
	4	86	0.3	5.0	1.6	>90	>50	1.05-1.25	>1.25	-	-	-	>90	0.45	0.25-0.75	0.35-0.65
	5	99	0.3	10.7	1.8	>90	15-65	0.90-1.05	0.9-2.0	>90	>70	4.25-4.75	>90	0.10	0.4-0.5	0.46-0.55
Total	930	0.3	10.7	1.9	>90	15-60	0.78-0.82	1.2-2.0	>90	>65	3.6-4.1	>90	0.10	0.45-0.65	0.51-0.59	
1:5,000	1	1059	14.4	1759.3	97.9	<90	15-20	0.013	40-50	>90	>25	2.2-3.1	<90	0.10	4.3-4.5	0.63-0.72
	2	896	4.8	1315.6	85.0	<90	10-20	0.016	40	>90	>25	2.4-3.2	<90	0.5	4.25	0.67-0.70
	3	299	5.3	1265.5	80.0	<90	10-20; 40-55	0.017; 0.015	40; 60	>90	25-35; >60	2.6; 2.8-3.4	<90	0.5	4.2	0.65-0.7
	4	832	8.1	1014.3	96.3	<90	10-40; 55-65	0.013; 0.0115	45; 80	>90	45-55; >70	2.6; 2.9	<90	0.5	4.3	0.7
	5	749	11.8	2306.4	121.2	<90	25	0.01	60	>90	>30	2.4-2.8	<90	0.20	4.5-4.8	0.65-0.77
Total	3791	4.8	2306.4	97.9	-	-	-	-	-	>90	>45	2.4-3.2	<90	0.40	4.3-4.7	0.55-0.75
1:25,000	1	216	88.7	1681.5	434.8	>90	>5	0.0036-0.0043	200	>90	-	-	>90	0.5	5.5-6	0.45-0.55
	2	187	61.2	1264.1	322.2	>90	>10	0.0045-0.0052	175	>90	-	-	>90	0.5	5.6-5.7	0.54-0.57
	3	62	105.0	1678.7	331.4	>90	0-10; >75	0.0045; 0.003	125; 275	>90	15-70	2.6-2.9	>90	-	-	-
	4	187	79.0	2652.4	395.9	>90	10-70	0.0038-0.004	200-400	>90	>75	3.6-3.8	>90	0.5	5.8-5.9	0.55-0.57
	5	242	89.9	1946.3	468.9	>90	5-75	0.0032-0.0037	250	>90	>80	3.8-4.6	>90	0	6	0.55
Total	894	61.2	2652.4	405.2	>90	>10	0.0034-0.004	200	-	-	-	>90	0.5	5.8-6	0.55-0.57	
1:100,000	1	48	312.5	1892.8	749.4	>90	>35	0.0029-0.0034	650	>90	-	-	>90	0.30	6.5-6.7	0.34-0.41
	2	48	226.2	2683.6	809.9	>90	0-15; 30-90	0.0016-0.0019	300	>90	-	-	>90	20-25	6.7	0.5
	3	5	400.4	1586.0	870.9	-	-	-	-	-	-	-	-	-	-	-
	4	45	208.5	3936.9	816.5	-	-	-	-	-	-	-	-	-	-	-
	5	103	250.0	3224.7	1034.9	>90	>15	0.0016-0.0018	300	>90	-	-	>90	0.10	6.8-6.9	0.47-0.55
Total	249	208.5	3936.9	893.7	>90	>10	0.0017-0.00185	400	-	-	-	>90	0.5	6.7-6.8	0.5-0.55	

435

4.5. Lineament density and intensity

436

As also suggested by the variation of the relative proportions of the dominant orientation sets across

437

the scales (Fig. 5a-b), also the normalized density P_{20} (m^{-2}) and intensity P_{21} (m/m^2) of each fracture

438

set vary across scales. The variations of density and intensity are both described by a power-law

439

relationship in log-log diagrams plotting the scale on the X-axis (e.g., $10^5 = 1:100,000$) and the

440

density P_{20} or intensity P_{21} on the Y-axis (Fig. 7a-b) (e.g., Castaing et al., 1996). The variation trend

441

for the total lineament density P_{20} of each map at different scales is characterized by power-law

442

exponents $\beta = -1.77$, which also corresponds to the average of the exponent values of all the other

443

lineament sets (Fig. 7a). Sets 1, 2 and 3 display β values larger than the average value; Sets 4 and 5

444

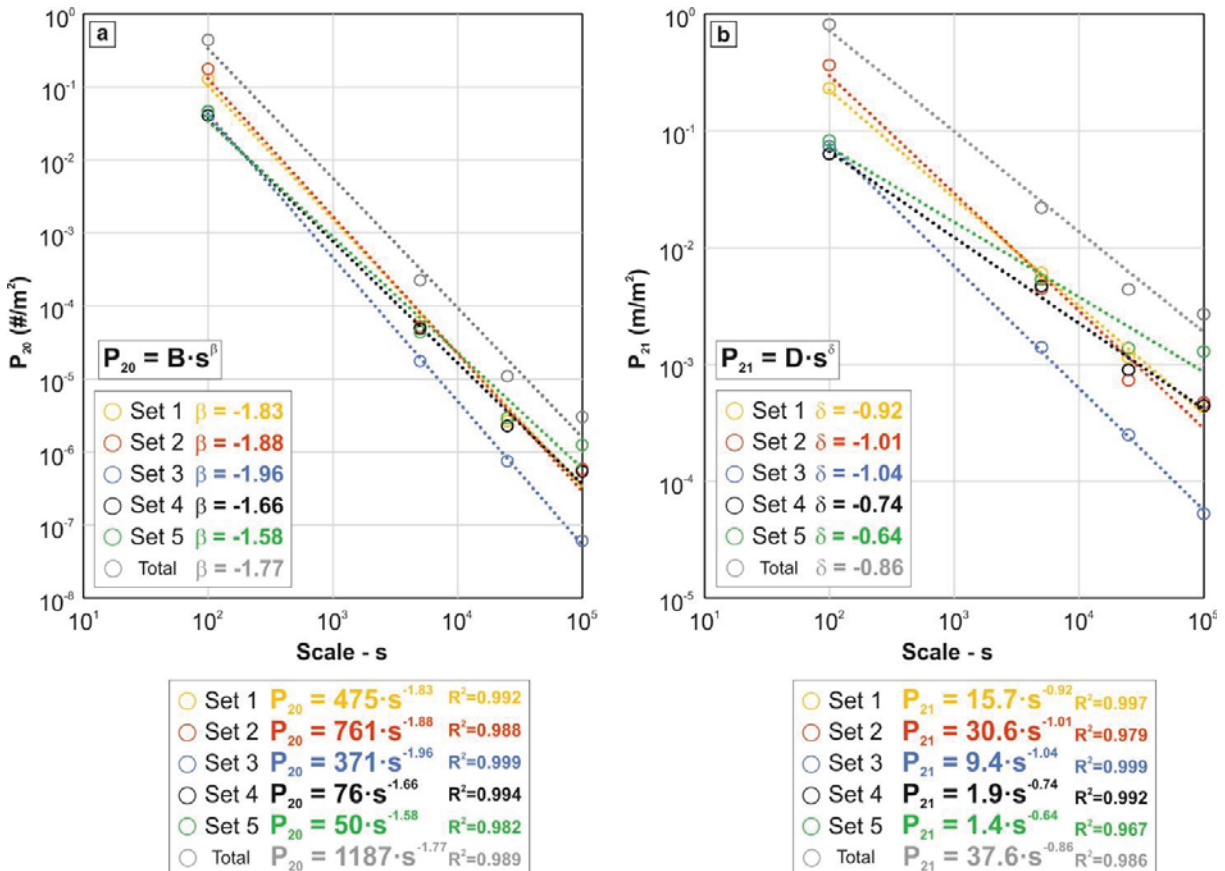
display β values smaller than the average values. Similarly, the variation trend for P_{21} is

445

characterized by a power-law exponent $\delta = -0.86$ (Fig. 7b); Sets 1, 2 and 3 show values of δ larger

446

than the average value. Sets 4 and 5 display δ values smaller than the average value.



447

448 **Figure 7.**

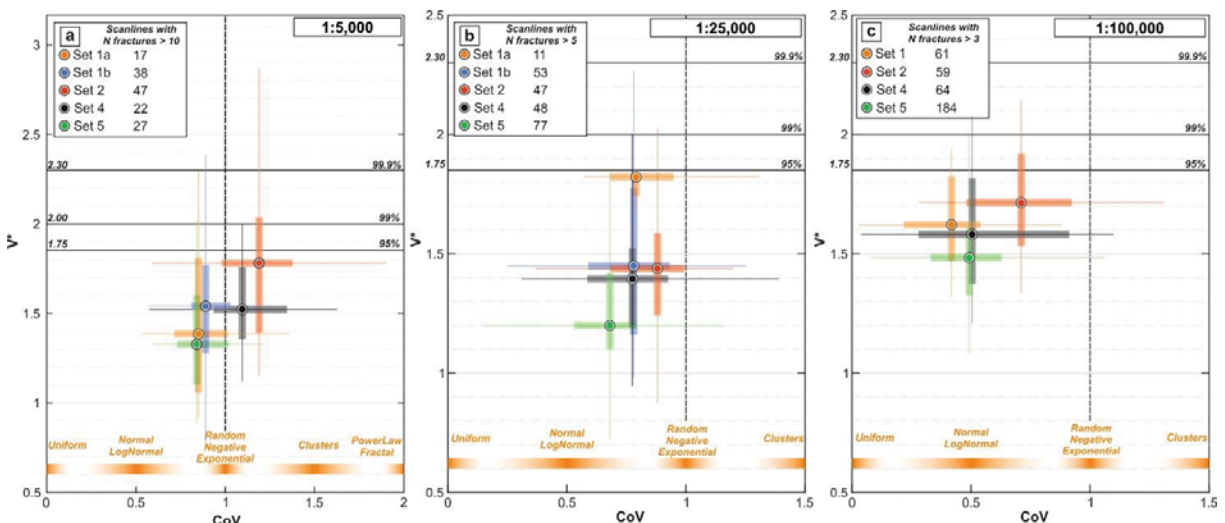
449 Lineament density (P_{20}) and intensity (P_{21}) variation across scales of each orientation set.

450

451 *4.6. Spacing and organization at different scales*

452 The spatial organization of fracture sets has been qualitatively estimated by comparing the values of
 453 the heterogeneity parameter V_f , its statistical significance level V^* and the Coefficient of Variation
 454 CoV for the scanlines performed in NetworkGT (Fig. 8; Table 3). At the 1:5,000 scale (Fig. 8a),
 455 scanlines intersecting both Set 1a and 1b lineaments are characterized by $CoV \leq 1$ and $V^* < 1.75$.
 456 This suggests that Set 1 may express a random-to-uniform spatial distribution. The same is
 457 observed at smaller scales (Fig. 8b-c), where CoV for Set 1 decreases on average, suggesting an
 458 even more random-to-uniform distribution. Set 2 lineaments display CoV on average >1 at the
 459 1:5,000 scale, and $V^* > 1.75$ for more than half of the observed values. This might suggest that Set 2
 460 lineaments are characterized by a clustered spatial distribution at the 1:5,000 scale. At smaller
 461 scales, both CoV and V^* values generally decrease, although some of the analyzed scanlines still
 462 display $CoV > 1$ and $V^* > 1.75-2.00$. Set 3 lineaments are too scattered and sparse to allow for a
 463 meaningful analysis of their spatial arrangement and, therefore, they are not reported in Fig. 8. Set 4
 464 lineaments mapped at the 1:5,000 scale on average show CoV values >1 , but V^* is rarely >1.75 . At
 465 smaller scales, both CoV and V^* decrease progressively. CoV and V^* for Set 5 lineaments are
 466 generally <1 and <1.75 , respectively, at each scale of observation.

467



468

469 **Figure 8.**

470 CoV-V* spatial organization diagrams for the orientation sets identified in the lineament map at (a)

471 1:5,000; (b) 1:25,000; and (c) 1:100,000 scale.

Scale	Set	1:5,000			1:25,000			1:100,000			
		Spacing (m)	CoV	V*	Spacing (m)	CoV	V*	Spacing (m)	CoV	V*	
		N>10: 17			N>5: 59			N>3: 61			
	1a	Avg	132.64	0.91	1.45	622.20	0.80	1.64	738.25	0.42	1.40
		Std dev	78.55	0.28	0.43	394.10	0.27	0.27	314.96	0.22	0.21
		Min	19.37	0.53	0.92	52.09	0.24	1.07	262.68	0.03	1.03
		Max	232.39	1.69	2.30	1568.75	1.42	2.01	1253.90	0.88	1.80
		N>10: 38			N>5: 106			-			
	1b	Avg	189.33	0.93	1.55	487.49	0.68	1.49	-	-	-
		Std dev	52.19	0.18	0.37	175.44	0.26	0.35	-	-	-
		Min	87.87	0.57	0.78	133.91	0.12	0.98	-	-	-
		Max	311.72	1.44	2.38	883.45	1.25	2.26	-	-	-
		N>10: 47			N>5: 122			N>3: 59			
	2	Avg	133.39	1.21	1.78	637.66	0.71	1.50	1013.41	0.71	1.52
		Std dev	45.48	0.32	0.44	512.73	0.27	0.27	304.75	0.28	0.27
		Min	37.64	0.59	1.15	89.24	0.09	0.87	352.64	0.28	1.05
		Max	213.61	2.02	2.87	2195.76	1.26	2.12	1506.44	1.31	2.05
		N>10: 22			N>5: 150			N>3: 64			
	4	Avg	135.66	1.10	1.54	403.84	0.69	1.44	671.34	0.50	1.34
		Std dev	41.33	0.29	0.27	238.35	0.23	0.27	403.20	0.26	0.28
		Min	75.78	0.57	1.12	72.51	0.22	0.82	150.10	0.04	0.89
		Max	251.38	1.62	2.00	1013.70	1.51	2.01	1566.48	1.10	1.96
		N>10: 27			N>5: 261			N>3: 184			
	5	Avg	150.88	0.89	1.36	404.46	0.58	1.36	453.89	0.49	1.23
		Std dev	69.94	0.23	0.31	219.18	0.25	0.26	174.28	0.22	0.26
		Min	51.16	0.60	0.88	83.31	0.08	0.72	52.05	0.08	0.72
		Max	255.16	1.62	2.02	1005.32	1.24	2.07	963.48	1.06	1.88

472

473 **Table 3.**

474 Spacing, CoV and V* statistical parameters.

475

476

477 **5. Discussion**

478 In the following, we firstly assess the scaling laws and exponent values obtained for the Bømlo
479 fracture network as well as their implications upon the classification of lineaments as geological
480 structures (e.g., fracture and fault zones). Then, we discuss the implications related to applying the
481 retrieved scaling relationships to the quantification of fracturing and reservoir permeability at
482 different scales. In addition, we evaluate the possible causes behind the observed discrepancy
483 between the results of multiscale and single-scale parameter quantifications.

484 *5.1. Characterization of geometric properties of the Bømlo fracture network*

485 The fractal dimensions D retrieved from the analysis of 2D lineament maps cluster around 1.5 (Fig.
486 4), similar to what is commonly reported from other case studies on fracture pattern fractal
487 dimensions (Bonnet et al., 2001; Hirata, 1989). Also, the normalized cumulative distribution of
488 fracture lengths effectively defines a single scaling law, which can be best described by a power-
489 law relationship with an exponent $\alpha = -1.95$ (Fig. 6a; Table 4). The general scaling law obtained for
490 the overall fracture network is very similar to that derived from many other case studies of fracture
491 networks affecting both crystalline basements and (meta)sedimentary rocks, with an average power-
492 law exponent very close to $\alpha = -2$ (cf. Bertrand et al., 2015; Bonnet et al., 2001; Bossennec et al.,
493 2021; Chabani et al., 2021; Le Garzic et al., 2011; McCaffrey et al., 2020; Odling, 1997; Torabi &
494 Berg, 2011). Similarly, the power-law scaling relationship defined by the fracture density P_{20} values
495 is characterized by a power-law exponent $\beta = -1.77$, similar to the value of -1.7 commonly observed
496 in many other fault networks (Castaing et al., 1996; Bonnet et al., 2001, and references therein).

497 These two features (similar fractal dimension and power-law scaling relationship) are commonly
498 used as evidence for the occurrence of a fracture network whose geometrical properties (size of
499 fractures, i.e., length, and spatial correlation and organization) are scale-invariant (Bonnet et al.,
500 2001). This suggests that, at a first approximation, the documented fracture pattern in the crystalline
501 basement of Bømlo is self-similar at any scale of observation. However, the Bømlo case may be

502 more complex than it would seem at a first glance. The Bømlø fracture network is composed of five
503 main orientation sets with variable relative abundance, density and intensity across scales (Figs. 5
504 and 7, Table 1). The observed variations of density and intensity are predictable and can be
505 described by a general power-law scaling, the exponent of which is characteristic of each
506 orientation set (Fig. 7; Table 4). Even though the cumulative length distribution for each orientation
507 set at each observation scale can be best approximated by other scaling laws than power-law (Table
508 2), the cumulative length distribution across scale is best approximated by a power-law scaling
509 relationship (Fig. 5b; Table 4). Again, each orientation set is characterized by its own power-law
510 exponent (Fig. 5b; Table 4), which differs slightly from that computed for the entire fracture
511 network.

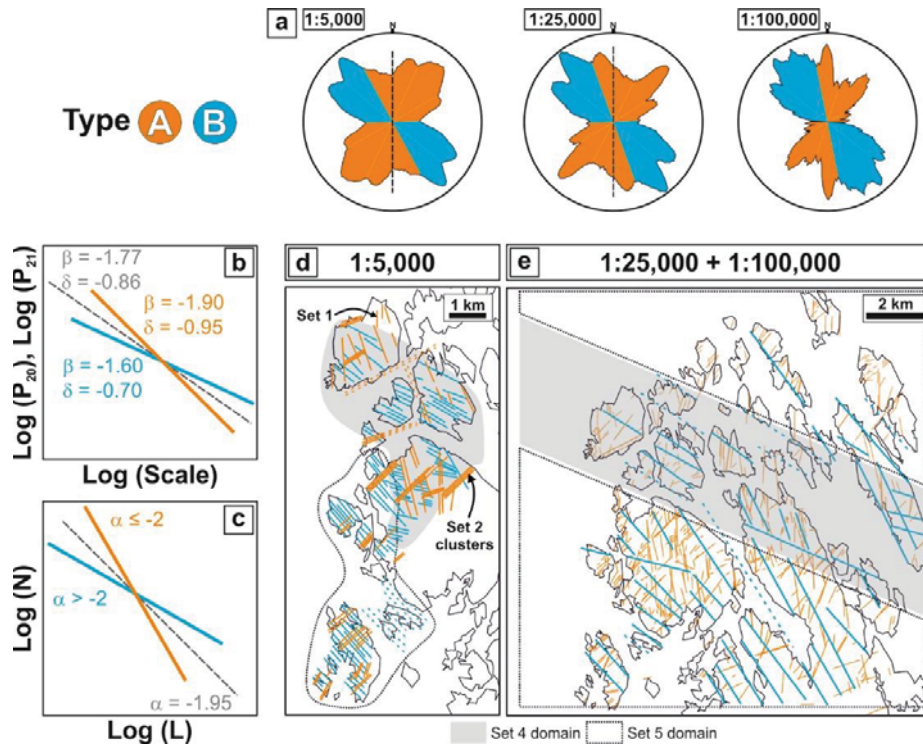
512 These variations of density and intensity of orientation sets across scales could be related to changes
513 in resolution of the digital representation of the terrain (DTMs and orthophotos) with a changing
514 scale of observation (Scheiber et al., 2015). However, conversely to what reported here, the change
515 in resolution would affect each orientation set equally, thus maintaining a constant relative
516 abundance across scales. Another possible bias affecting the identification of fractures at different
517 scales may result from the constant direction of the light source adopted for the LiDAR DTM
518 hillshading (light source from NW in this case). Likely, this may affect the detection of lineaments
519 at specific orientations, but systematic effects have not been identified by previous studies (Scheiber
520 et al., 2015).

521 Nevertheless, some fracture sets clearly display similar trends of variation of the relative abundance
522 and intensity, such that they can be grouped into two main set types (Fig. 9; Table 4): (1) Type A
523 includes Sets 1, 2 and 3, characterized by comparable P_{20} and P_{21} variation trends across scales,
524 with similar β and δ exponents close to -1.90 and -0.95, respectively – their relative abundance
525 decreases from 1:100 to 1:100,000 scale (Fig. 9a-b); (2) Type B includes Sets 4 and 5, with a
526 comparable variation trend in intensity, characterized by $\beta \approx -1.60$ and $\delta \approx -0.70$, and a similar

527 variation of the relative abundance across scales, showing an increasing fracture intensity from
528 1:100 to 1:100,000 scale (Fig. 9a-b). The sorting into Type A and B is also justified by the power-
529 law exponents of the general cumulative length distribution for each fracture set (Figs. 6b, 9c; Table
530 4). Type A fracture sets are characterized by a power-law exponent α close to -2 or smaller. Type B
531 fracture sets, instead, are characterized by power-law exponents >-2 . Whereas this is true for Set 5
532 ($\alpha = -1.68$), it is rather difficult to find a general power-law relation that encompasses the entire set
533 of scales of observation for Set 4 (see Fig. Supplement S3). The cumulative length distributions also
534 show that the longest lineaments, those of likely regional significance observed at small scale
535 (1:25,000, 1:100,000), belong to Type B sets.

536 This classification into Type A and B fracture sets is not directly reflected in the CoV-V* diagrams
537 that quantify the spatial organization of fracture sets (Fig. 8a-b). Conversely to all the other
538 analyzed parameters, even though the fracture network as a whole presents scale-invariant
539 geometrical features as suggested by the rather constant fractal dimension D , the spatial
540 organization of its constituent components, that is, the individual fracture sets, seems to be scale-
541 dependent. As a consequence, we can infer that the spacing distribution of fractures belonging to
542 each fracture set is scale-dependent. The CoV-V* diagrams highlight a similar decreasing trend for
543 all the analyzed fracture sets with increasing scale of observation (from 1:100,000 to 1:5,000). The
544 most significant variation across scales in the spatial distribution occurs for Set 2 and Set 4, both
545 of which exhibit a tendency to occur as clusters at the large scale (1:5,000; $\text{CoV} > 1$, $V^* > 1.75$;
546 Figs. 8a-9d), whereas they are randomly-to-uniformly distributed at the smaller scales (1:25,000
547 and 1:100,000; $\text{CoV} < 1$; $V^* < 1.75$; Figs. 8b-c, 9e). Set 1 (a & b) and Set 5 are randomly-to-
548 uniformly distributed at all scales of observations ($\text{CoV} < 1$; $V^* < 1.75$; Figs. 8, 9d-e). None of the
549 analyzed fracture sets show a tendency to develop fractal behavior with a power-law spacing
550 distribution. Therefore, the analyzed fracture sets appear to display a hierarchical organization
551 within a fracture network presenting overall scale-invariant geometrical properties (e.g., Le Garzic

552 et al., 2011). In it, Type B lineaments represent the higher-order structures, controlling the
 553 geometrical properties of the network at the regional scale (Fig. 9d-e). The schematic representation
 554 of lineaments in Fig. 9 highlights an heterogeneous distribution of Type B lineaments, which is not
 555 captured by the statistical analysis of spacing heterogeneity. Indeed, the Rolvsnes granodiorite can
 556 be subdivided into several domains of the lineament maps where either Set 4 or Set 5 fractures are
 557 predominant at the regional scale (“Set 4-5 domain” – grey and dashed transparent areas in Fig. 9d-
 558 e). On the other hand, Type A lineaments represent lower-order structures and control the
 559 geometrical properties of the network at the local-to-outcrop scale (Fig. 9d-e).



560

561 **Figure 9.**

562 Schematic summary of the results for the Bømlo case study. (a) Rose diagrams of the orientation of
 563 lineaments at different scales (1:5,000; 1:25,000; 1:100,000) with the classification into Type A and
 564 B lineaments. (b) Schematic log-log diagram showing the observed general trends of P_{20} and P_{21}
 565 variations with scale. The values of β and δ exponents are reported for the entire fracture network
 566 (grey dashed line), Type A (orange line) and Type B (light blue line) lineaments. (c) Schematic log-

567 log diagram showing the observed general scaling laws retrieved for the cumulative length
 568 distributions. The values of the exponent α are reported for the entire fracture network (grey dashed
 569 line), Type A (orange line) and Type B (light blue line) lineaments. (d) Schematic representation of
 570 the fracture distribution at 1:5,000 scale. The reported lineament are redrawn from the 1:5,000
 571 lineament map and represent the actual spatial organization observed at Bømlo. Note the clustered
 572 organization of Set 2 fractures and the two domains (highlighted by transparent grey and dashed
 573 areas) where Set 4 and Set 5 fractures are dominant, respectively. (e) Schematic representation of
 574 the fracture distribution at 1:25,000–1:100,000 scales. The reported lineaments are redrawn from
 575 the 1:25,000–1:100,000 lineament maps and represent the actual spatial organization mapped on
 576 Bømlo.

577

	Set Type	Cumulative length distributions		P20 density distribution			P21 intensity distribution		
		$N(l > L) = A \cdot L^\alpha$		$P_{20} = B \cdot s^\beta$			$P_{21} = D \cdot s^\delta$		
		A	α	B	β	R^2	D	δ	R^2
Set 1	A	0.2	-2	475	-1.83	0.992	15.7	-0.92	0.997
Set 2	A	0.3	-2.15	761	-1.88	0.988	30.6	-1.01	0.979
Set 3	A	0.04	-2	371	-1.96	0.999	9.4	-1.04	0.999
Set 4	B	0.5	-2.2	76	-1.66	0.994	1.9	-0.74	0.992
Set 5	B	0.04	-1.68	50	-1.58	0.982	1.4	-0.64	0.967
578 Total		0.6	-1.95	1187	-1.77	0.989	37.6	-0.86	0.986

579 **Table 4.**

580 Summary table reporting the power-law scaling and the values of the related parameters retrieved
 581 from the multiscale analysis of cumulative length distribution, fracture density and intensity.

582

583

584 *5.2. General power-law scaling for the fracture network and fracture sets: implications*
585 *and limitations*

586 The fracture network exhibits some general power-law relationships describing the multiscale
587 behavior of both length distribution ($\alpha = -1.95$), fracture density P_{20} ($\beta = -1.77$) and fracture
588 intensity P_{21} ($\delta = -0.86$) (Table 4). These general power-law scaling laws may effectively be
589 adopted to retrieve fracture network properties (geometrical properties and permeability) at any
590 scale of observation. However, the adoption of a general scaling law for the geometrical properties,
591 without taking into consideration the peculiarity of each fracture set building up the fracture
592 network, may lead to an erroneous extrapolation of the analyzed properties. In particular, for our
593 case study, significant deviations would occur in the upscaling/downscaling of fracture density P_{20}
594 and intensity P_{21} . As shown in Figs. 5 and 6, fracture sets exhibit different power-law exponents,
595 which are systematically smaller for Sets 1, 2 and 3 (Type A), and larger for Sets 4 and 5 (Type B)
596 than the exponent of the fracture network taken as a whole. By adopting power-law exponents
597 larger than the actual exponent of the fracture set would lead to an overestimation of the fracture
598 network properties at larger scales. Vice-versa, adopting power-law exponents smaller than the
599 actual exponent of the fracture set would lead to an underestimation of the density/intensity/length
600 distribution at larger scale. In the case of the Bømlø fracture network, this
601 overestimation/underestimation can be significant and it can reach one order of magnitude in terms
602 of fracture intensity and density (Fig. 7).

603 In addition, field investigations (Ceccato, Viola, Antonellini, et al., 2021; Ceccato, Viola, Tartaglia,
604 et al., 2021; Scheiber & Viola, 2018) have revealed the highly heterogeneous distribution of
605 fractures at the outcrop scale. Only for some orientation sets, fractures are homogeneously
606 distributed over the studied outcrop (e.g., Sets C-D of Ceccato et al., 2021a, corresponding to Sets
607 3-4 reported here). Most of the identified fracture sets at the outcrop present, instead, either a
608 clustered spatial organization or a variable intensity over short distances (50-100 m). This

609 represents of course a limitation to the extrapolation of the general power-law identified in this
610 study, and thus the lower bound for the application of the proposed power-law scaling (Bonnet et
611 al., 2001). Similarly, the heterogeneous spatial distribution of Set 4 and 5 fractures identified at
612 small scale of observation (Fig. 9d-e) needs to be accounted for when evaluating the upper limit of
613 applicability of the general scaling laws defined here.

614 The outcrop-scale spatial heterogeneity and the overestimation/underestimation effects of applying
615 a general power-law scaling become relevant when considering the role that different fracture sets
616 may have in the definition of the net permeability of fractured crystalline basement. As highlighted
617 by field studies (Ceccato, Viola, Antonellini, et al., 2021; Ceccato, Viola, Tartaglia, et al., 2021;
618 Gabrielsen & Braathen, 2014), each fracture set may contribute differently to the bulk permeability
619 of the fractured crystalline basement. Fracture clusters and minor normal faults may represent
620 effective fluid pathways at the outcrop scale, which well represents the sub-seismic resolution scale
621 (Ceccato, Viola, Tartaglia, et al., 2021; Place et al., 2016; Souque et al., 2019). On the other hand,
622 fault zones may control fluid flow and reservoir compartmentalization at the regional scale
623 (Holdsworth et al., 2019). Accordingly, any underestimation/overestimation of their density and
624 their organized spatial distribution may deeply affect the accuracy of hydrological and petrophysical
625 models of the fractured basement at the outcrop and at its sub-seismic resolution scale (Bertrand et
626 al., 2015; Le Garzic et al., 2011).

627 The retrieved power-law relationship may thus effectively represent a powerful tool to enhance the
628 prediction and visualization of SSRS structural features, which normally remain beyond the
629 resolution offered by standard (large-scale seismic investigations) and high-resolution (local-scale
630 surficial investigations, e.g., ground penetrating radar, electrical resistivity tomography)
631 geophysical methods. These mathematical relationships provide the opportunity to infer the
632 occurrence and the spatial heterogeneity of SSRS structures that are critical in controlling the
633 permeability of fractured crystalline basement.

634 *5.3. Interpretation of the Bømlo fracture network in the regional framework*

635 We have shown that, as a whole, the granodioritic crystalline basement on Bømlo is characterized
636 by a scale-invariant fracture network, composed of different fracture sets with a variable spatial
637 organization across scales (Fig. 9). At the smallest scale, this fracture network is dominated by the
638 homogeneously-spaced, WNW-to-NW-striking Set 4 and Set 5 lineaments (Type B; Fig. 9d-e).
639 These lineaments are characteristic of and predominant over the whole of western and southwestern
640 Norway onshore (Gabrielsen et al., 2002; Gabrielsen & Braathen, 2014), as well as offshore (Preiss
641 & Adam, 2021). The general computed power-law exponent ($\alpha > -2$) suggests that long fractures
642 represent a substantial part of the overall fracture population of Type B lineaments. This also
643 suggests that Type B lineaments probably represent localized zones accommodating significant
644 deformation, when compared to Type A structures (Ackermann et al., 2001). Therefore, these
645 lineaments probably represent major fractures and normal fault zones formed and repeatedly
646 reactivated during the prolonged brittle tectonic history of the Rolvsnes granodiorite forming the
647 crystalline basement of Bømlo (Ceccato, Viola, Antonellini, et al., 2021; Preiss & Adam, 2021;
648 Scheiber & Viola, 2018; Viola et al., 2016). At the largest analyzed scale, the fracture network is
649 mainly dominated by random-to-clustered, NNW-SSE to NE-SW-striking fracture sets (Type A,
650 Sets 1 & 2; Fig. 9d-e). These structures are mainly related to minor faults and mineralized veins
651 (Set 2), fracture clusters and normal fault zones (Set 1) (cf. Gabrielsen and Braathen, 2014;
652 Scheiber and Viola, 2018). Accordingly, the general power-law exponent ($\alpha < -2$) suggests that
653 among Type A lineaments, short fractures represent a significant part of the lineament population,
654 probably resulting from an early stage of distributed faulting and deformation accommodation
655 (Ackermann et al., 2001).

656 The fractured and weathered crystalline basement of Bømlo, and in particular the Rolvsnes
657 granodiorite, is generally considered as the onshore analogue of the crystalline basement of the
658 Utsira High located offshore in the northern North Sea (Trice et al., 2019). Our results can,

659 therefore, provide invaluable insights on the geometry and spatial organization of the fractures
660 within the crystalline basement of the fractured basement reservoir buried below the North Sea
661 sedimentary cover (Fredin et al., 2017; Preiss & Adam, 2021). To extrapolate our results to the
662 offshore fractured basement, however, one needs to also consider several other factors deeply
663 affecting the development of fractures and fault zones regionally. First of all, the Utsira High and
664 the Bømlo crystalline basement blocks resided at different structural levels during the North Sea
665 rifting history, them being at the center and on the shoulder of the rift system, respectively
666 (Scheiber & Viola, 2018). Thus, they may have been subject to significantly different deformation
667 intensity and regimes (Bell et al., 2014). Accordingly, the length distribution, density, and intensity
668 of the identified Type A and B lineaments offshore might significantly differ from those presented
669 here. In addition, care must be taken when extrapolating and comparing these results to the regional
670 framework. Indeed, structural inheritance, the occurrence of intra-basement structures and the
671 lithological-mechanical anisotropy of the (poly)-metamorphic crystalline basement of southwestern
672 Norway deeply affect the intensity and geometry of fracture networks at the local and regional
673 scales (Fazlikhani et al., 2017; Fossen et al., 2017; Gabrielsen et al., 2018; Osagiede et al., 2020;
674 Phillips et al., 2016; Preiss & Adam, 2021). This structural inheritance may lead to significant
675 differences in the geometry and scaling properties of the fracture network when compared with
676 those described for the Rolvsnes granodiorite.

677 *5.4. Comparison between MLE-KS results and qualitative multiscale fitting (General*
678 *scaling law)*

679 MLE-KS statistical tests have already demonstrated their strength in the analysis of fault attribute
680 distribution (Dichiarante et al., 2020; Kolyukhin & Torabi, 2013). In our case, the results of length
681 cumulative distributions fitting with MLE-KS tests differ significantly from the general power-law
682 qualitative relation defined by comparing multiscale cumulative distributions. Similar to what
683 reported by Dichiarante et al. (2020), non-truncated cumulative length distributions are best fitted

684 by log-normal functions (see fitting scores <90 for log-normal functions in Table 2). Even when the
685 distribution is best approximated by a power-law function (e.g., most fracture sets mapped at
686 1:5,000; Table 2), the values of the power-law exponents retrieved from MLE-KS tests ($\alpha > -2$)
687 differ from those obtained from the fitting of multiscale distributions ($\alpha = -1.95$).

688 These deviations (both that from the power-law at each scale and that of the power-law exponents
689 from the general ones) are commonly observed in almost all natural fracture networks. Remarkable
690 deviations from a power-law scaling behavior have been previously explained as resulting from
691 several causes: (i) analytical biases (such as truncation and censoring of lineaments interpreted from
692 DTMs) (Manzocchi et al., 2009; Odling, 1997; Yielding et al., 1996); (ii) subdivision of long
693 lineaments into segments (segmentation) (Ackermann et al., 2001; Cao & Lei, 2018; Scholz, 2002;
694 Schultz et al., 2013; Xu et al., 2006); (iii) effectively different scaling properties at different scales
695 of observation (Castaing et al., 1996; Le Garzic et al., 2011; Kruhl, 2013).

696 Justifying the observed deviation from power-law scaling at a specific scale of observation only by
697 referring to truncation and censoring biases would mean that, in most cases, the dataset is in most
698 part ($\gg 50\%$) biased (see upper cut values $> 65\%$ for power-law fitting where negative exponential
699 functions best approximate the cumulative distributions in Table 2), and thus of little use to any
700 kind of statistically significant analysis.

701 Segmentation of long lineaments into shorter segments may be due to several causes, both
702 introduced into the dataset by analytical/interpretative biases, and intrinsically related to the genetic
703 fracture formation processes. Segmentation may result from partial exposure and cover of the
704 fracture network, and it may decrease the power-law scaling exponent, without affecting the type
705 of scaling-law function (Cao & Lei, 2018). Segmentation may be related to the progressive growth
706 stages of fault/joint patterns evolving with increasing accommodated deformation and faulting
707 maturity from a network composed of completely isolated short fractures to a network formed by a
708 few long, single lineaments, through fracture interaction and interconnection (Ackermann et al.,

709 2001; Michas et al., 2015; Scholz, 2002). This has been demonstrated to affect both the shape of the
710 mathematical function describing the length distribution (exponential vs. power-law), as well as the
711 power-law exponent at a specific scale of observation (Schultz et al., 2013). However, this may
712 explain the difference in scaling relationships observed during the evolution of a fracture network
713 through time and not at different scales of observation. In addition, the subjective choice of tracing
714 single segments composing a longer lineament as separate fractures rather than tracing a single,
715 continuous, long lineament, may likely affect the cumulative length distributions of the fracture
716 network. Tracing single segments would increase the number of short segments compared to longer
717 segments, at constant P_{21} intensity, increasing the total number of traced lineaments, and thus
718 decreasing the power-law exponent of the distribution (Xu et al., 2006). This segmentation bias may
719 justify the fact that power-law exponents of the multiscale length distributions of each fracture set
720 (Fig. 5b) are systematically smaller than those obtained from MLE-KS tests at 1:5,000 scale.
721 Whether or not this sampling bias may effectively affect the mathematical shape of the cumulative
722 distribution would deserve further investigations, which go beyond the scope of the present paper.

723 That fracture networks may effectively present different scaling properties at different scales of
724 observations thus seems to be the most plausible option (Kruhl, 2013). Indeed, fault and fracture
725 networks may present a hierarchical organization, which inherently implies scale-dependent
726 geometrical properties and spatial distribution of lineaments (Castaing et al., 1996; Le Garzic et al.,
727 2011). In fact, this is also consistent with the observed variation of relative abundances of
728 orientation sets across scales: each lineament set contributes differently to the overall fracture
729 network geometrical characters and thus the variation of the relative abundance may also lead to
730 variations in geometrical properties (spatial organization and length distributions) at different scales
731 (e.g., Le Garzic et al., 2011). Nevertheless, the combination of fracture sets with scale-dependent
732 properties (e.g. spatial organization or length distribution functions) may result in a fracture

733 network responding to power-law scaling laws, which could be described as a fractal, scale-
734 invariant fracture network (Bonnet et al., 2001).

735 **6. Conclusions**

736 The fractured crystalline basement of the Rolvsnes granodiorite on Bømlo is characterized by the
737 occurrence of a fractal fracture network controlled by a general power-law scaling law for the
738 distribution of fracture lengths. However, detailed orientation-dependent analyses have revealed
739 that this first-approximation scale-invariant fracture network is composed of fracture sets, which
740 individually exhibit a scale-dependent hierarchical spatial distribution, and parameter variation
741 trends with the scale of observation. Different trends of intensity/density variation across scales for
742 each orientation set have been detected, as well as different scaling laws for length distribution of
743 each orientation set. These observations may suggest that the documented fracture network results
744 from the summation of different geological structures (e.g., faults vs. joints, major fault zones vs.
745 incipient minor faults), organized in a hierarchical manner and characterized by different
746 geometrical and scale-dependent properties.

747 Our study allows us to draw some general conclusions about the methods of characterization of
748 fracture network and their analysis:

749 - First of all, the presented multiscale analytical workflow may represent a valid option for the
750 quantification of large, inherently incomplete (due to analytical and subjective biases)
751 lineament datasets. The lineament maps retrieved from digital terrain and surface models of
752 the Bømlo crystalline basement offer very large datasets, which are inherently incomplete
753 due to partial exposure and/or incomplete sampling of lineament due to resolution or human
754 bias (Scheiber et al., 2015). Thus a statistical approach such as that proposed in this paper is
755 highly recommended when aiming to retrieve relevant information from datasets that, for
756 several reasons, are only partially representative of the entire fracture network.

- 757 - Detailed orientation-dependent, multiscale analyses of the fracture network can provide the
758 different scaling laws and geometrical properties for each constituent fracture set, which can
759 be adopted to improve the detail and tune the accuracy of models of sub-seismic-resolution
760 scale structural features and the associated permeability in fractured crystalline basements.
- 761 - The integration of multiscale length distribution analyses, multiscale intensity/density
762 estimations and multiscale description of spatial organization provides useful information
763 for the classification of topographic lineaments as different geological structures (e.g.,
764 fracture/joint corridors vs fault zones) with specific hierarchy and control on the
765 permeability of the fractured basement.

766

767 **Acknowledgments**

768 Our research work was funded by the still ongoing BASE 2 project (“Basement fracturing and
769 weathering onshore and offshore Norway—Genesis, age, and landscape development” – Part 2) and
770 BASE 3 (NFR grant number 319849), a research initiative launched and steered by the Geological
771 Survey of Norway and supported by Equinor ASA, Aker BP ASA, Lundin Energy Norway AS,
772 Spirit Energy Norway AS, Wintershall Dea Norge, and NGU. We thank all BASE colleagues for
773 continuous discussion and constructive inputs. Roberto Emanuele Rizzo is warmly thanked for
774 fruitful discussions. Eric James Ryan is thanked for field support and the acquisition of UAV-drone
775 imagery. The Authors declare they have no perceived financial conflicts of interests with respect to
776 the results of this paper.

777 **Data Availability**

778 Data analyzed (shapefiles of manually picked lineaments and related geometrical properties) in the
779 present paper are available at: (“Multiscale_lineament_analyses_dataset”, Mendeley Data, V1, doi:
780 10.17632/4zdjpmr9jk.1).

782 **References**

- 783 Achtziger-Zupančič, P., Loew, S., & Mariéthoz, G. (2017). A new global database to improve
784 predictions of permeability distribution in crystalline rocks at site scale. *Journal of*
785 *Geophysical Research: Solid Earth*, *122*(5), 3513–3539.
786 <https://doi.org/10.1002/2017JB014106>
- 787 Ackermann, R. V., Schlische, R. W., & Withjack, M. O. (2001). The geometric and statistical
788 evolution of normal fault systems: an experimental study of the effects of mechanical layer
789 thickness on scaling laws. *Journal of Structural Geology*, *23*(11), 1803–1819.
790 [https://doi.org/10.1016/S0191-8141\(01\)00028-1](https://doi.org/10.1016/S0191-8141(01)00028-1)
- 791 Andrews, B., Roberts, J., Shipton, Z., Bigi, S., Tartarello, M. C., & Johnson, G. (2019). How do we
792 see fractures? Quantifying subjective bias in fracture data collection. *Solid Earth*, *10*(2), 487–
793 516. <https://doi.org/10.5194/SE-10-487-2019>
- 794 Bell, R. E., Jackson, C. A. L., Whipp, P. S., & Clements, B. (2014). Strain migration during
795 multiphase extension: Observations from the northern North Sea. *Tectonics*, *33*(10), 1936–
796 1963. <https://doi.org/10.1002/2014TC003551>
- 797 Bertrand, L., Géraud, Y., Le Garzic, E., Place, J., Diraison, M., Walter, B., & Haffen, S. (2015). A
798 multiscale analysis of a fracture pattern in granite: A case study of the Tamariu granite,
799 Catalunya, Spain. *Journal of Structural Geology*, *78*, 52–66.
800 <https://doi.org/10.1016/j.jsg.2015.05.013>
- 801 Bistacchi, A., Mitterpergher, S., Martinelli, M., & Storti, F. (2020). On a new robust workflow for
802 the statistical and spatial analysis of fracture data collected with scanlines (or the importance of
803 stationarity). *Solid Earth*, *11*(6), 2535–2547. <https://doi.org/10.5194/SE-11-2535-2020>
- 804 Bonnet, E., Bour, O., Odling, N. E., Davy, P., Main, I., Cowie, P., & Berkowitz, B. (2001). Scaling
805 of fracture systems in geological media. *Reviews of Geophysics*, *39*(3), 347–383.

806 <https://doi.org/10.1029/1999RG000074>

807 Bossennec, C., Frey, M., Seib, L., Bär, K., & Sass, I. (2021). Multiscale characterisation of fracture
808 patterns of a crystalline reservoir analogue. *Geosciences (Switzerland)*, *11*(9), 1–23.

809 <https://doi.org/10.3390/geosciences11090371>

810 Brace, W. F. (1984). Permeability of Crystalline Rocks: New in Situ Measurements. *Journal of*
811 *Geophysical Research*, *89*(B6), 4327–4330. <https://doi.org/10.1029/jb089ib06p04327>

812 Cao, W., & Lei, Q. (2018). Influence of Landscape Coverage on Measuring Spatial and Length
813 Properties of Rock Fracture Networks: Insights from Numerical Simulation. *Pure and Applied*

814 *Geophysics*, *175*(6), 2167–2179. <https://doi.org/10.1007/s00024-018-1774-4>

815 Castaing, C., Halawani, M. A., Gervais, F., Chilès, J. P., Genter, A., Bourguine, B., et al. (1996).

816 Scaling relationships in intraplate fracture systems related to Red Sea rifting. *Tectonophysics*,

817 *261*(4), 291–314. [https://doi.org/10.1016/0040-1951\(95\)00177-8](https://doi.org/10.1016/0040-1951(95)00177-8)

818 Ceccato, A., Viola, G., Antonellini, M., Tartaglia, G., & Ryan, E. J. (2021). Constraints upon fault
819 zone properties by combined structural analysis of virtual outcrop models and discrete fracture

820 network modelling. *Journal of Structural Geology*, *152*(September), 104444.

821 <https://doi.org/10.1016/j.jsg.2021.104444>

822 Ceccato, A., Viola, G., Tartaglia, G., & Antonellini, M. (2021). In-situ quantification of mechanical
823 and permeability properties on outcrop analogues of offshore fractured and weathered

824 crystalline basement: Examples from the Rolvsnes granodiorite, Bømlo, Norway. *Marine and*

825 *Petroleum Geology*, *124*(July 2020). <https://doi.org/10.1016/j.marpetgeo.2020.104859>

826 Chabani, A., Trullenque, G., Ledésert, B. A., & Klee, J. (2021). Multiscale characterization of
827 fracture patterns: A case study of the noble hills range (Death valley, CA, Usa), application to

828 geothermal reservoirs. *Geosciences (Switzerland)*, *11*(7), 25–27.

829 <https://doi.org/10.3390/geosciences11070280>

- 830 Damsleth, E., Sangolt, V., & Aamodt, G. (1998). Sub-seismic faults can seriously affect fluid flow
831 in the Njord field off Western Norway - A stochastic fault modeling case study. *Proceedings -*
832 *SPE Annual Technical Conference and Exhibition, 1999-Septe*, 295–304.
833 <https://doi.org/10.2523/49024-ms>
- 834 Dershowitz, W. S., & Herda, H. H. (1992). Interpretation of fracture spacing and intensity. *The 33rd*
835 *U.S. Symposium on Rock Mechanics (USRMS), Santa Fe, New Mexico, June 1992.*, 757–766.
836 Retrieved from [http://onepetro.org/ARMAUSRMS/proceedings-pdf/ARMA92/All-](http://onepetro.org/ARMAUSRMS/proceedings-pdf/ARMA92/All-ARMA92/ARMA-92-0757/1987502/arma-92-0757.pdf)
837 [ARMA92/ARMA-92-0757/1987502/arma-92-0757.pdf](http://onepetro.org/ARMAUSRMS/proceedings-pdf/ARMA92/All-ARMA92/ARMA-92-0757/1987502/arma-92-0757.pdf)
- 838 Dichiarante, A. M., McCaffrey, K. J. W., Holdsworth, R. E., Bjørnarå, T. I., & Dempsey, E. D.
839 (2020). Fracture attribute scaling and connectivity in the Devonian Orcadian Basin with
840 implications for geologically equivalent sub-surface fractured reservoirs. *Solid Earth*, *11*(6),
841 2221–2244. <https://doi.org/10.5194/se-11-2221-2020>
- 842 Fazlikhani, H., Fossen, H., Gawthorpe, R. L., Faleide, J. I., & Bell, R. E. (2017). Basement
843 structure and its influence on the structural configuration of the northern North Sea rift.
844 *Tectonics*, *36*(6), 1151–1177. <https://doi.org/10.1002/2017TC004514>
- 845 Fossen, H., Khani, H. F., Faleide, J. I., Ksienzyk, A. K., & Dunlap, W. J. (2016). Post-Caledonian
846 extension in the West Norway-northern North Sea region: The role of structural inheritance.
847 *Geological Society Special Publication*, *439*(1), 465–486. <https://doi.org/10.1144/SP439.6>
- 848 Fossen, H., Khani, H. F., Faleide, J. I., Ksienzyk, A. K., & Dunlap, W. J. (2017). Post-Caledonian
849 extension in the West Norway-northern North Sea region: The role of structural inheritance.
850 *Geological Society Special Publication*, *439*(1), 465–486. <https://doi.org/10.1144/SP439.6>
- 851 Fossen, H., Ksienzyk, A. K., Rotevatn, A., Bauck, M. S., & Wemmer, K. (2021). From widespread
852 faulting to localised rifting: Evidence from K-Ar fault gouge dates from the Norwegian North
853 Sea rift shoulder. *Basin Research*, *33*(3), 1934–1953. <https://doi.org/10.1111/BRE.12541>

- 854 Fredin, O., Viola, G., Zwingmann, H., Sørli, R., Brønner, M., Lie, J. E., et al. (2017). The
855 inheritance of a mesozoic landscape in western Scandinavia. *Nature Communications*, 8.
856 <https://doi.org/10.1038/ncomms14879>
- 857 Gabrielsen, R. H., & Braathen, A. (2014). Models of fracture lineaments - Joint swarms, fracture
858 corridors and faults in crystalline rocks, and their genetic relations. *Tectonophysics*, 628, 26–
859 44. <https://doi.org/10.1016/j.tecto.2014.04.022>
- 860 Gabrielsen, R. H., Braathen, A., Dehis, J., & Roberts, D. (2002). Tectonic lineaments of Norway.
861 *Norsk Geologisk Tidsskrift*, 82(3), 153–174.
- 862 Gabrielsen, R. H., Nystuen, J. P., & Olesen, O. (2018). Fault distribution in the Precambrian
863 basement of South Norway. *Journal of Structural Geology*, 108, 269–289.
864 <https://doi.org/10.1016/j.jsg.2017.06.006>
- 865 Le Garzic, E., de L'Hamaide, T., Diraison, M., Géraud, Y., Sausse, J., de Urreiztieta, M., et al.
866 (2011). Scaling and geometric properties of extensional fracture systems in the proterozoic
867 basement of Yemen. Tectonic interpretation and fluid flow implications. *Journal of Structural*
868 *Geology*, 33(4), 519–536. <https://doi.org/10.1016/j.jsg.2011.01.012>
- 869 Gee, D. G., Fossen, H., Henriksen, N., & Higgins, A. K. (2008). From the early Paleozoic platforms
870 of Baltica and Laurentia to the Caledonide Orogen of Scandinavia and Greenland. *Episodes*,
871 31(1), 44–51. <https://doi.org/10.18814/epiiugs/2008/v31i1/007>
- 872 Gillespie, P. A., Howard, C. B., Walsh, J. J., & Watterson, J. (1993). Measurement and
873 characterisation of spatial distributions of fractures. *Tectonophysics*, 226(1–4), 113–141.
874 [https://doi.org/10.1016/0040-1951\(93\)90114-Y](https://doi.org/10.1016/0040-1951(93)90114-Y)
- 875 Hardebol, N. J., Maier, C., Nick, H., Geiger, S., Bertotti, G., & Boro, H. (2015). Multiscale fracture
876 network characterization and impact on flow: A case study on the Latemar carbonate platform.
877 *Journal of Geophysical Research: Solid Earth*, 120(12), 8197–8222.

- 878 <https://doi.org/10.1002/2015JB011879>
- 879 Healy, D., Rizzo, R. E., Cornwell, D. G., Farrell, N. J. C., Watkins, H., Timms, N. E., et al. (2017).
880 FracPaQ: A MATLABTM toolbox for the quantification of fracture patterns. *Journal of*
881 *Structural Geology*, 95, 1–16. <https://doi.org/10.1016/j.jsg.2016.12.003>
- 882 Hirata, T. (1989). Fractal Dimension of Fault Systems in Japan: Fractal Structure in Rock Fracture
883 Geometry at Various Scales. *Fractals in Geophysics*, 157–170. [https://doi.org/10.1007/978-3-](https://doi.org/10.1007/978-3-0348-6389-6_9)
884 [0348-6389-6_9](https://doi.org/10.1007/978-3-0348-6389-6_9)
- 885 Holdsworth, R. E., McCaffrey, K. J. W., Dempsey, E., Roberts, N. M. W., Hardman, K., Morton,
886 A., et al. (2019). Natural fracture propping and earthquake-induced oil migration in fractured
887 basement reservoirs. *Geology*, 47(8), 700–704. <https://doi.org/10.1130/G46280.1>
- 888 Holdsworth, R. E., Trice, R., Hardman, K., McCaffrey, K. J. W., Morton, A., Frei, D., et al. (2020).
889 The nature and age of basement host rocks and fissure fills in the Lancaster field fractured
890 reservoir, West of Shetland. *Journal of the Geological Society*, jgs2019-142.
891 <https://doi.org/10.1144/jgs2019-142>
- 892 Kolyukhin, D., & Torabi, A. (2013). Power-Law Testing for Fault Attributes Distributions. *Pure*
893 *and Applied Geophysics* 2013 170:12, 170(12), 2173–2183. [https://doi.org/10.1007/S00024-](https://doi.org/10.1007/S00024-013-0644-3)
894 [013-0644-3](https://doi.org/10.1007/S00024-013-0644-3)
- 895 Kruhl, J. H. (2013). Fractal-geometry techniques in the quantification of complex rock structures: A
896 special view on scaling regimes, inhomogeneity and anisotropy. *Journal of Structural*
897 *Geology*, 46, 2–21. <https://doi.org/10.1016/J.JSG.2012.10.002>
- 898 Laubach, S. E., Olson, J. E., & Cross, M. R. (2009). Mechanical and fracture stratigraphy. *AAPG*
899 *Bulletin*, 93(11), 1413–1426. <https://doi.org/10.1306/07270909094>
- 900 Lundmark, A. M., Sæther, T., & Sørli, R. (2014). Ordovician to silurian magmatism on the Utsira

- 901 High, North Sea: Implications for correlations between the onshore and offshore Caledonides.
902 *Geological Society Special Publication*, 390(1), 513–523. <https://doi.org/10.1144/SP390.21>
- 903 Manzocchi, T., Walsh, J. J., & Bailey, W. R. (2009). Population scaling biases in map samples of
904 power-law fault systems. *Journal of Structural Geology*, 31(12), 1612–1626.
905 <https://doi.org/10.1016/J.JSG.2009.06.004>
- 906 Marrett, R., Gale, J. F. W., Gómez, L. A., & Laubach, S. E. (2018). Correlation analysis of fracture
907 arrangement in space. *Journal of Structural Geology*, 108, 16–33.
908 <https://doi.org/10.1016/J.JSG.2017.06.012>
- 909 McCaffrey, K. J. W., Holdsworth, R. E., Pless, J., Franklin, B. S. G., & Hardman, K. (2020).
910 Basement reservoir plumbing: fracture aperture, length and topology analysis of the Lewisian
911 Complex, NW Scotland. *Journal of the Geological Society*.
912 <https://doi.org/https://doi.org/10.1144/jgs2019-143> This
- 913 Michas, G., Vallianatos, F., & Sammonds, P. (2015). Statistical mechanics and scaling of fault
914 populations with increasing strain in the Corinth Rift. *Earth and Planetary Science Letters*,
915 431, 150–163. <https://doi.org/10.1016/J.EPSL.2015.09.014>
- 916 Munro, M. A., & Blenkinsop, T. G. (2012). MARD-A moving average rose diagram application for
917 the geosciences. *Computers and Geosciences*, 49, 112–120.
918 <https://doi.org/10.1016/j.cageo.2012.07.012>
- 919 Nyberg, B., Nixon, C. W., & Sanderson, D. J. (2018). NetworkGT: A GIS tool for geometric and
920 topological analysis of two-dimensional fracture networks. *Geosphere*, 14(4), 1618–1634.
921 <https://doi.org/10.1130/GES01595.1>
- 922 Odling, N. E. (1997). Scaling and connectivity of joint systems in sandstones from western Norway.
923 *Journal of Structural Geology*, 19(10), 1257–1271. <https://doi.org/10.1016/S0191->
924 8141(97)00041-2

- 925 Odling, N. E., Gillespie, P., Bourguine, B., Castaing, C., Chilés, J. P., Christensen, N. P., et al.
926 (1999). Variations in fracture system geometry and their implications for fluid flow in
927 fractured hydrocarbon reservoirs. *Petroleum Geoscience*, 5(4), 373–384.
928 <https://doi.org/10.1144/petgeo.5.4.373>
- 929 Osagiede, E. E., Rotevatn, A., Gawthorpe, R., Kristensen, T. B., Jackson, C. A. L., & Marsh, N.
930 (2020). Pre-existing intra-basement shear zones influence growth and geometry of non-
931 colinear normal faults, western Utsira High–Heimdal Terrace, North Sea. *Journal of Structural*
932 *Geology*, 130, 103908. <https://doi.org/10.1016/J.JSG.2019.103908>
- 933 Pennacchioni, G., Ceccato, A., Fioretti, A. M., Mazzoli, C., Zorzi, F., & Ferretti, P. (2016).
934 Episyenites in meta-granitoids of the Tauern Window (Eastern Alps): unpredictable? *Journal*
935 *of Geodynamics*, 101. <https://doi.org/10.1016/j.jog.2016.04.001>
- 936 Phillips, T. B., Jackson, C. A. L., Bell, R. E., Duffy, O. B., & Fossen, H. (2016). Reactivation of
937 intrabasement structures during rifting: A case study from offshore southern Norway. *Journal*
938 *of Structural Geology*, 91, 54–73. <https://doi.org/10.1016/J.JSG.2016.08.008>
- 939 Place, J., Géraud, Y., Diraison, M., Herquel, G., Edel, J. B., Bano, M., et al. (2016). Structural
940 control of weathering processes within exhumed granitoids: Compartmentalisation of
941 geophysical properties by faults and fractures. *Journal of Structural Geology*, 84, 102–119.
942 <https://doi.org/10.1016/j.jsg.2015.11.011>
- 943 Preiss, A. D., & Adam, J. (2021). Basement fault trends in the Southern North Sea Basin. *Journal of*
944 *Structural Geology*, 153, 104449. <https://doi.org/10.1016/J.JSG.2021.104449>
- 945 Riber, L., Dypvik, H., & Sørli, R. (2015). Altered basement rocks on the Utsira High and its
946 surroundings, Norwegian North Sea. *Norwegian Journal of Geology*, 95(1), 57–89.
947 <https://doi.org/10.17850/njg95-1-04>
- 948 Rizzo, R. E., Healy, D., & De Siena, L. (2017). Benefits of maximum likelihood estimators for

- 949 fracture attribute analysis: Implications for permeability and up-scaling. *Journal of Structural*
950 *Geology*, 95, 17–31. <https://doi.org/10.1016/j.jsg.2016.12.005>
- 951 Sanderson, D. J., & Peacock, D. C. P. (2019). Line sampling of fracture swarms and corridors.
952 *Journal of Structural Geology*, 122(December 2018), 27–37.
953 <https://doi.org/10.1016/j.jsg.2019.02.006>
- 954 Scheiber, T., & Viola, G. (2018). Complex Bedrock Fracture Patterns: A Multipronged Approach to
955 Resolve Their Evolution in Space and Time. *Tectonics*, 37(4), 1030–1062.
956 <https://doi.org/10.1002/2017TC004763>
- 957 Scheiber, T., Fredin, O., Viola, G., Jarna, A., Gasser, D., & Łapińska-Viola, R. (2015). Manual
958 extraction of bedrock lineaments from high-resolution LiDAR data: methodological bias and
959 human perception. *Gff*, 137(4), 362–372. <https://doi.org/10.1080/11035897.2015.1085434>
- 960 Scheiber, T., Viola, G., Wilkinson, C. M., Ganerød, M., Skår, Ø., & Gasser, D. (2016).
961 Direct⁴⁰Ar/³⁹Ar dating of Late Ordovician and Silurian brittle faulting in the southwestern
962 Norwegian Caledonides. *Terra Nova*, 28(5), 374–382. <https://doi.org/10.1111/ter.12230>
- 963 Schneeberger, R., Egli, D., Lanyon, G. W., Mäder, U. K., Berger, A., Kober, F., & Herwegh, M.
964 (2018). Structural-permeability favorability in crystalline rocks and implications for
965 groundwater flow paths: a case study from the Aar Massif (central Switzerland). *Hydrogeology*
966 *Journal*, 26(8), 2725–2738. <https://doi.org/10.1007/s10040-018-1826-y>
- 967 Scholz, C. H. (2002). *The Mechanics of Earthquakes and Faulting (Second edition)*. Cambridge
968 University Press. Retrieved from
969 <http://books.google.com/books?hl=en%7B&%7Damp;lr=%7B&%7Damp;id=JL1VM5wMbrQC%7B&%7Damp;oi=fnd%7B&%7Damp;pg=PR11%7B&%7Damp;dq=The+mechanics+of+earthquakes+and+faulting%7B&%7Damp;ots=tDcZRs3p2x%7B&%7Damp;sig=M-vxuJ99fg0ez086EuTvxsPvQJs>

- 973 Schultz, R. A., Klimczak, C., Fossen, H., Olson, J. E., Exner, U., Reeves, D. M., & Soliva, R.
974 (2013). Statistical tests of scaling relationships for geologic structures. *Journal of Structural*
975 *Geology*, 48, 85–94. <https://doi.org/10.1016/J.JSG.2012.12.005>
- 976 Slagstad, T., Davidsen, B., & Stephen Daly, J. (2011). Age and composition of crystalline basement
977 rocks on the norwegian continental margin: Offshore extension and continuity of the
978 Caledonian-Appalachian orogenic belt. *Journal of the Geological Society*, 168(5), 1167–1185.
979 <https://doi.org/10.1144/0016-76492010-136>
- 980 Soliva, R., Benedicto, A., & Maerten, L. (2006). Spacing and linkage of confined normal faults:
981 Importance of mechanical thickness. *Journal of Geophysical Research: Solid Earth*, 111(B1),
982 1402. <https://doi.org/10.1029/2004JB003507>
- 983 Souque, C., Knipe, R. J., Davies, R. K., Jones, P., Welch, M. J., & Lorenz, J. (2019). Fracture
984 corridors and fault reactivation: Example from the Chalk, Isle of Thanet, Kent, England.
985 *Journal of Structural Geology*, 122(March 2015), 11–26.
986 <https://doi.org/10.1016/j.jsg.2018.12.004>
- 987 Stober, I., & Bucher, K. (2015). Hydraulic conductivity of fractured upper crust: Insights from
988 hydraulic tests in boreholes and fluid-rock interaction in crystalline basement rocks. *Geofluids*,
989 15(1–2), 161–178. <https://doi.org/10.1111/gfl.12104>
- 990 Tanner, D. C., Buness, H., Igel, J., Günther, T., Gabriel, G., Skiba, P., et al. (2019). *Fault detection.*
991 *Understanding Faults: Detecting, Dating, and Modeling*. [https://doi.org/10.1016/B978-0-12-](https://doi.org/10.1016/B978-0-12-815985-9.00003-5)
992 [815985-9.00003-5](https://doi.org/10.1016/B978-0-12-815985-9.00003-5)
- 993 Tartaglia, G., Viola, G., van der Lelij, R., Scheiber, T., Ceccato, A., & Schönenberger, J. (2020).
994 “Brittle structural facies” analysis: A diagnostic method to unravel and date multiple slip
995 events of long-lived faults. *Earth and Planetary Science Letters*, 545, 116420.
996 <https://doi.org/10.1016/j.epsl.2020.116420>

- 997 Torabi, A., & Berg, S. S. (2011). Scaling of fault attributes: A review. *Marine and Petroleum*
998 *Geology*, 28(8), 1444–1460. <https://doi.org/10.1016/j.marpetgeo.2011.04.003>
- 999 Trice, R., Hiorth, C., & Holdsworth, R. (2019). Fractured basement play development on the UK
1000 and Norwegian rifted margins. *Geological Society, London, Special Publications*, SP495-
1001 2018–174. <https://doi.org/10.1144/sp495-2018-174>
- 1002 Viola, G., Scheiber, T., Fredin, O., Zwingmann, H., Margreth, A., & Knies, J. (2016).
1003 Deconvoluting complex structural histories archived in brittle fault zones. *Nature*
1004 *Communications*, 7, 1–10. <https://doi.org/10.1038/ncomms13448>
- 1005 Walsh, J. J., Watterson, J., Heath, A., Gillespie, P. A., & Childs, C. (1998). Assessment of the
1006 effects of sub-seismic faults on bulk permeabilities of reservoir sequences. *Geological Society*
1007 *Special Publication*, 127, 99–114. <https://doi.org/10.1144/GSL.SP.1998.127.01.08>
- 1008 Xu, S.-S., Nieto-Samaniego, A. F., Alaniz-Álvarez, S. A., & Velasquillo-Martínez, L. G. (2006).
1009 Effect of sampling and linkage on fault length and length–displacement relationship.
1010 *International Journal of Earth Sciences* 2005 95:5, 95(5), 841–853.
1011 <https://doi.org/10.1007/S00531-005-0065-3>
- 1012 Yielding, G., Needham, T., & Jones, H. (1996). Sampling of fault populations using sub-surface
1013 data: A review. *Journal of Structural Geology*, 18(2–3), 135–146.
1014 [https://doi.org/10.1016/S0191-8141\(96\)80039-3](https://doi.org/10.1016/S0191-8141(96)80039-3)
- 1015